ORGANIC PROCESS RESEARCH & DEVELOPMENT
OPR&D

pubs.acs.org/OPRD Article

A Virtual Plant for Integrated Continuous Manufacturing of a Carfilzomib Drug Substance Intermediate, Part 3: Manganese-Catalyzed Asymmetric Epoxidation, Crystallization, and Filtration

Andrew J. Maloney, Elçin Içten,* Gerard Capellades, Matthew G. Beaver, Xiaoxiang Zhu, Lauren R. Graham, Derek B. Brown, Daniel J. Griffin, Rahul Sangodkar, Ayman Allian, Seth Huggins, Roger Hart, Pablo Rolandi, Shawn D. Walker, and Richard D. Braatz

Cite This: *Org. Process Res. Dev.* 2020, 24, 1891−1908 Read Online

ACCESS | Metrics & More | Article Recommendations

ABSTRACT: This article describes the process characterization and development of models to inform a process control strategy to prepare (*R*,*R*)-epoxy ketone **2**, an intermediate in the manufacture of carfilzomib. Model calibration for relevant unit operations and the development of a dynamic integrated flowsheet-level model in gPROMS FormulatedProducts software enabled investigation of the impact of process disturbances and model uncertainties on the critical quality attributes (CQAs) and identification of critical process disturbances and failure modes to guide a process control strategy. The model development was similar to that described in the previous parts of this series, but with the added complexity of comparing two distinct kinetic formulations for the epoxidation reaction. The main CQAs for this process were (1) the conversion of enone **1** (target ≥99.0 mol % conversion) and (2) the purity target for solids prior to cake wash (target ≥97.5% purity by weight). Conversion of enone was not always achieved with the expected disturbances: whereas 99.5% conversion was expected for normal operating conditions, 97.2% conversion was predicted for the worst-case combination of disturbances. The chiral purity of crystalline (*R*,*R*)-epoxy ketone **2** was not always achieved with the expected disturbances: 98.2% purity was expected for normal operating conditions, and 96.7% purity was expected for the worst-case combination of disturbances. These analyses allowed for rank ordering of critical process parameters that impact conversion and suitable manipulated variables to develop a robust process control strategy for the manufacturing scheme.

KEYWORDS: *continuous pharmaceutical manufacturing, process modeling, flow chemistry, continuous crystallization, continuous filtration, advanced process control*

1. INTRODUCTION

Continuous manufacturing (CM) has gained interest from academia, regulatory agencies, and the pharmaceutical industry.[1−4] Capitalizing on this interest, Amgen has evaluated the implementation of CM for the production of a carfilzomib drug substance intermediate. The oxidation reaction detailed herein is of particular interest because the process requires exothermic and hazardous chemistries that are well-controlled in continuous operation.[5,6]

To aid in the development of this CM process, in silico modeling has been used to determine the process parameters (PPs) that most strongly impact the critical quality attributes (CQAs).[7,8] The adoption of such an approach is crucial because of the inherent interconnectedness of unit operations in continuous manufacturing.[9−11] Therefore, the work in this series of papers focuses on the development, experimental validation, and use of in silico models to support the development of a CM process.

Parts I and II of this series show the development of process models for the synthesis and purification of the morpholine amide (10.1021/acs.oprd.0c00187)[12] and enone **1** (10.1021/acs.oprd.0c00188),[13] respectively. Part III of this publication series continues with the development of a continuous manufacturing process to produce (*R*,*R*)-epoxy ketone **2** from enone **1** (Scheme 1) by manganese-catalyzed epoxidation using hydrogen peroxide as the stoichiometric oxidant.[14,15] A major challenge of this chemistry is its strongly exothermic nature, with a heat of reaction of almost −250 kJ/mol[16] and an adiabatic temperature rise (ART) of 60 °C. Another challenge addressed in this work is the undesired competing disproportionation of hydrogen peroxide by the manganese catalyst.[17] Following the reaction to synthesize (*R*,*R*)-epoxy ketone **2**, a number of workup steps, including liquid−liquid extraction, continuous crystallization, and filtration, are performed to separate and purify it. A mixed-suspension mixed-product-removal (MSMPR) continuous crystallization process, which has been demonstrated academically and industrially,[18−22] was developed. Similarly, filtration has also been demonstrated in industrial and academic settings, with various filtration schemes

Special Issue: Flow Chemistry Enabling Efficient Synthesis

Received: April 15, 2020
Published: July 14, 2020

Scheme 1. Synthesis of (*R,R*)-Epoxy Ketone 2 by Epoxidation of Enone 1

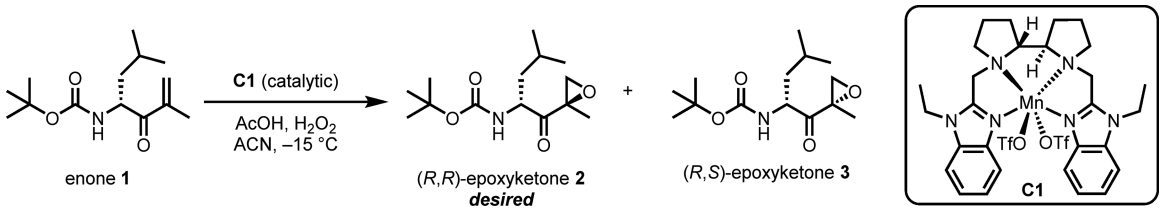

Scheme 2. Process Flow Diagram for the Step 3 Continuous Process

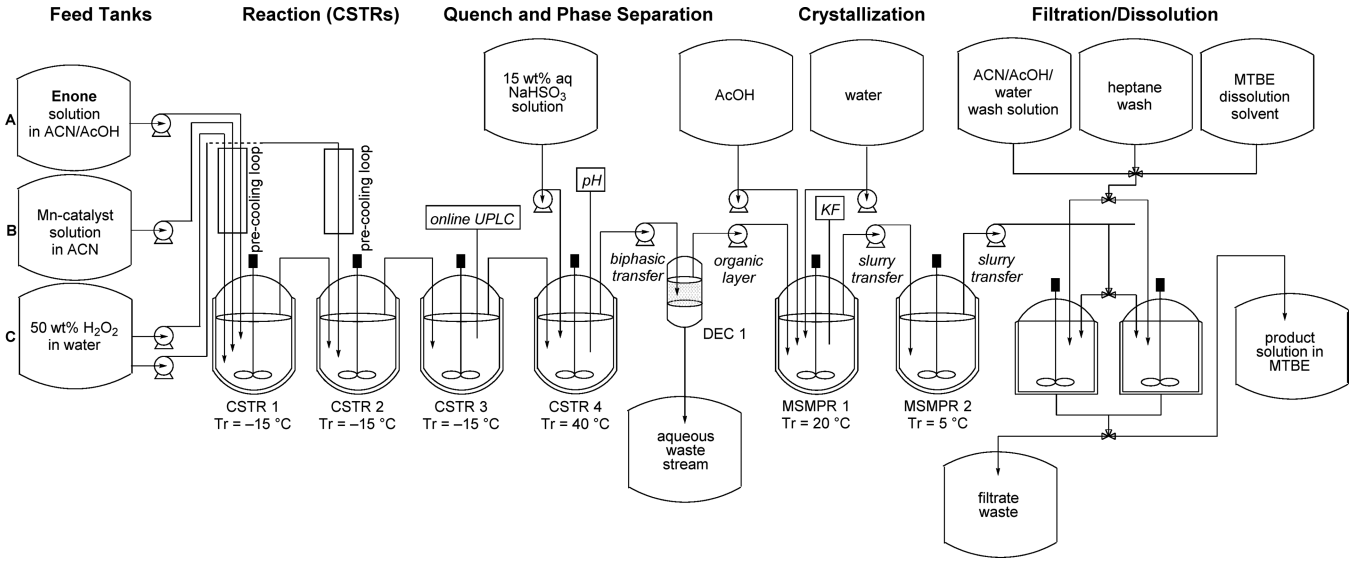

having been developed for CM processes.[20,21,23] Continuous filtration examples include (1) rotating porous plates and carousels for filtration, washing, and drying of isolated material and (2) parallel batchwise devices for filtration, washing, and dissolution of the cake, as employed in this work.[20,21,23] Process models were developed for all of the unit operations and used for in silico characterization of the integrated continuous process, which enabled the development and testing of an advanced process control strategy.

2. VIRTUAL PLANT DEVELOPMENT FOR THE SYNTHESIS OF (*R,R*)-EPOXY KETONE 2

The continuous manufacturing process for (*R,R*)-epoxy ketone **2** is illustrated in Scheme 2. The feed streams containing enone **2** in acetonitrile (ACN) and acetic acid (AcOH), Mn catalyst **C1** in ACN, and 50 wt % hydrogen peroxide (H_2O_2) in water are passed through precooling loops and combined to initiate the epoxidation process. The observation of gas evolution resulting from the disproportionation of H_2O_2 to form oxygen and water (vide infra) prompted the use of a continuously stirred tank reactor (CSTR) platform for this reaction sequence. The effluent of CSTR1 is sent to CSTR2 along with another stream of hydrogen peroxide. Additional aging is required in CSTR2 and CSTR3 prior to the quench with an aqueous solution of sodium bisulfite ($NaHSO_3$) in CSTR4 followed by phase separation in Decanter 1 (DEC1). The organic phase is sent to a two-stage MSMPR crystallization along with water and AcOH. The effluent of MSMPR crystallizer 1 (MSMPR1) is then sent to MSMPR2 for improved recovery of the (*R,R*)-epoxy ketone. The crystallized solids are then washed and isolated using two parallel filtration units. The solids are then dissolved in methyl *tert*-butyl ether (MTBE). This solution is then sent for the next step, not discussed herein, which includes the reaction with triazabicylodecene to form the (*S,R*)-epoxy ketone, which is then isolated via batch crystallization and filtration.[24]

Each unit operation in Scheme 2 was individually characterized to develop a mechanistic understanding of the relevant phenomena. An experimental plan was developed and executed to characterize each unit operation in batch mode for normal and abnormal operation. Data from this characterization were used to calibrate the model of each unit operation. The models were then integrated into an end-to-end flowsheet, which was used for disturbance analysis and the development of a process design and process control strategy to meet the desired specifications in the presence of these disturbances.

2.1. Process Characterization Experiments and Parameter Estimation for Model Development. *2.1.1. Product Formation: Reaction Kinetics and Kinetic Model Development.* Three key reactions occur in CSTR1. The first reaction, the formation of (*R,R*)-epoxy ketone **2**, involves the reaction of enone **1** and H_2O_2 as described in eq 1. The second reaction, formation of (*R,S*)-epoxy ketone **3**, the primary impurity, also involves the reaction of enone **1** and H_2O_2, as described in eq 2. The final reaction, disproportionation of H_2O_2 by the Mn catalyst, is shown in eq 3. The catalyst is homogeneous, and thus, all of the reactions are homogeneous as well.

$$\text{enone} + H_2O_2 \xrightarrow{\text{Mn}} (R,R)\text{-epoxy ketone} + H_2O \quad (1)$$

$$\text{enone} + H_2O_2 \xrightarrow{\text{Mn}} (R,S)\text{-epoxy ketone} + H_2O \quad (2)$$

$$H_2O_2 \xrightarrow{\text{Mn}} H_2O + \frac{1}{2}O_2 \quad (3)$$

https://dx.doi.org/10.1021/acs.oprd.0c00189
Org. Process Res. Dev. 2020, 24, 1891−1908

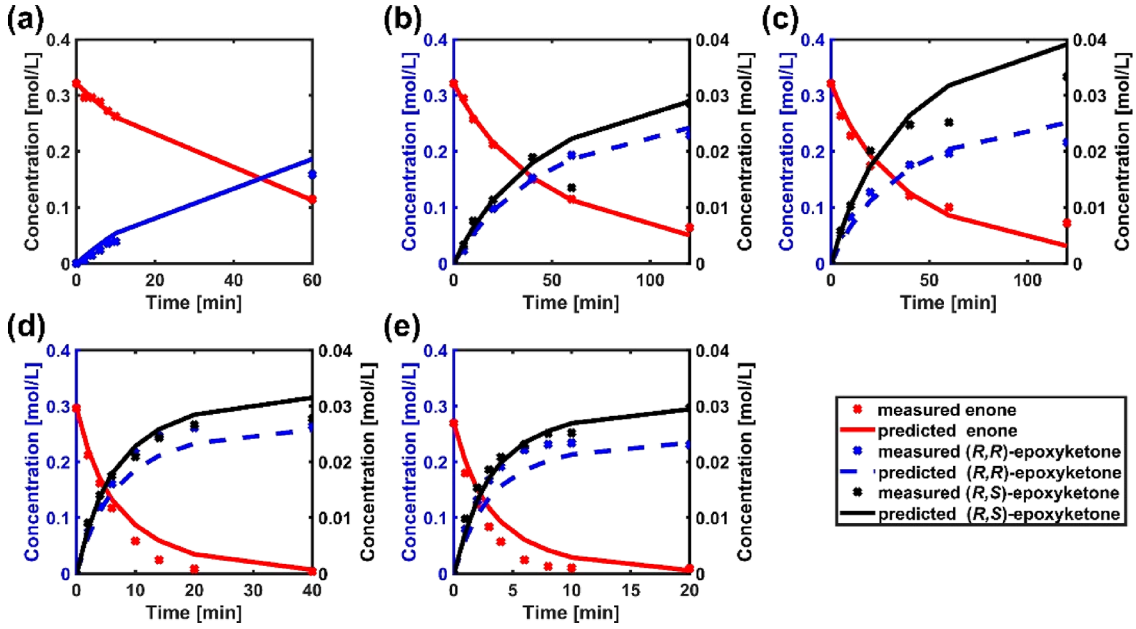

Figure 1. Comparison between model predictions without eq 3 characterized and experimental values for the enone, (*R*,*R*)-epoxy ketone, and (*R*,*S*)-epoxy ketone concentrations for (a) −18 °C and 0.01 mol % Mn catalyst, (b) −18 °C and 0.01 mol % Mn catalyst, (c) −8 °C and 0.01 mol % Mn catalyst, (d) −18 °C and 0.05 mol % Mn catalyst, and (e) −18 °C and 0.1 mol % Mn catalyst.

To characterize the reaction kinetics for the reactions shown in eqs 1 and 2, a set of batch kinetic experiments with reaction temperatures between −18 and −8 °C and Mn catalyst loadings between 0.01 and 0.1 mol % with respect to the enone were executed. The volumetric scale of the experiments was 1 to 2 mL of total reaction mixture to minimize the impact of the reaction exotherm, and time series data were collected in every reaction to track the depletion of enone **1** and the formation of (*R*,*R*)-epoxy ketone **2** and (*R*,*S*)-epoxy ketone **3** via high-performance liquid chromatography (HPLC), as shown in Figure 1. Aliquots of the reaction mixture were immediately quenched at the appropriate dilution with a room-temperature 1:1 ACN/water solution. Control experiments confirmed that the reaction was inhibited using this quench strategy.

The reaction was found to be first-order with respect to the reactants and four-thirds order with respect to the Mn catalyst concentration. The order with respect to the catalyst concentration was found by plotting the measured enone concentration as a function of time multiplied by the catalyst concentration for the experiments in Figure 1. The reaction order (four-thirds) corresponds to the condition under which the data fall onto a master curve, as the catalyst is not consumed in the reaction. While the mechanism for a four-thirds order with respect to Mn is not clear, this model describes the experimental observations well. The reaction rate constant (k_r) was modeled to have an Arrhenius temperature dependence (eq 4):

$$k_r = k \exp\left[-\frac{E_a}{R}\left(\frac{1}{T} - \frac{1}{T_{ref}}\right)\right] \quad (4)$$

where k is pre-exponential factor for the reaction, E_a is the activation energy, R is the universal gas constant, T_{ref} is the reference temperature, and T is the temperature at which the rate constant is to be determined. Values of the parameters are given in Table 1. This model was found to overpredict the conversion of the enone (i.e., the rates of the reactions given by eqs 1 and 2), presumably because of the exclusion of hydrogen peroxide decomposition in the model. Estimation of the kinetic parameters for the reaction shown in eq 3 was difficult because of the lack of analytical data to measure the products of this reaction.

Table 1. Regressed Kinetic Parameters of the Epoxidation Reaction without Hydrogen Peroxide Decomposition (T_{ref} = −18 °C)

reaction	rate constant $[(m^3/mol)^{n-1}\ s^{-1}]$	E_a (kJ/mol)
eq 1	$4.7 \times 10^{-5} \pm 2.8 \times 10^{-6}$	14 ± 7
eq 2	$5.3 \times 10^{-6} \pm 2.7 \times 10^{-7}$	29 ± 6

To characterize the hydrogen peroxide decomposition reaction, a set of batch kinetic experiments at −20 and 0 °C with 0.07 mol % Mn catalyst were designed and executed in a reaction calorimeter. Enone **1** was excluded from the reaction mixture to ensure that only eq 3 would occur. The large exotherm associated with this reaction and vigorous O_2 evolution challenged the characterization of this reaction. The volumetric scale of the experiments was 35 to 40 mL of total reaction mixture, and time series calorimetry data were collected and correlated to the depletion of hydrogen peroxide through its heat of reaction, as shown in Figure 2. The exothermicity of the process (97.48 kJ/mol of H_2O_2) resulted in temperature variations despite the use of a reaction calorimeter designed to ensure isothermal reaction performance. The runs at −20 °C were executed as technical replicates to understand the batch-to-batch variability, and no significant impact on the conversion was observed.

With these new data, the kinetic parameters for the reactions shown in eqs 1 and 2 were refit using the original experimental data, as shown in Figure 3. As before, the rates of the reactions shown in eqs 1 and 2 had a four-thirds order dependence on the catalyst concentration. While the agreement with the experimental data looks qualitatively similar in Figures 1 and 3, both the kinetic parameter estimates (Table 2) and predictive powers of the models are quite different. An implicit assumption of this

https://dx.doi.org/10.1021/acs.oprd.0c00189
Org. Process Res. Dev. 2020, 24, 1891−1908

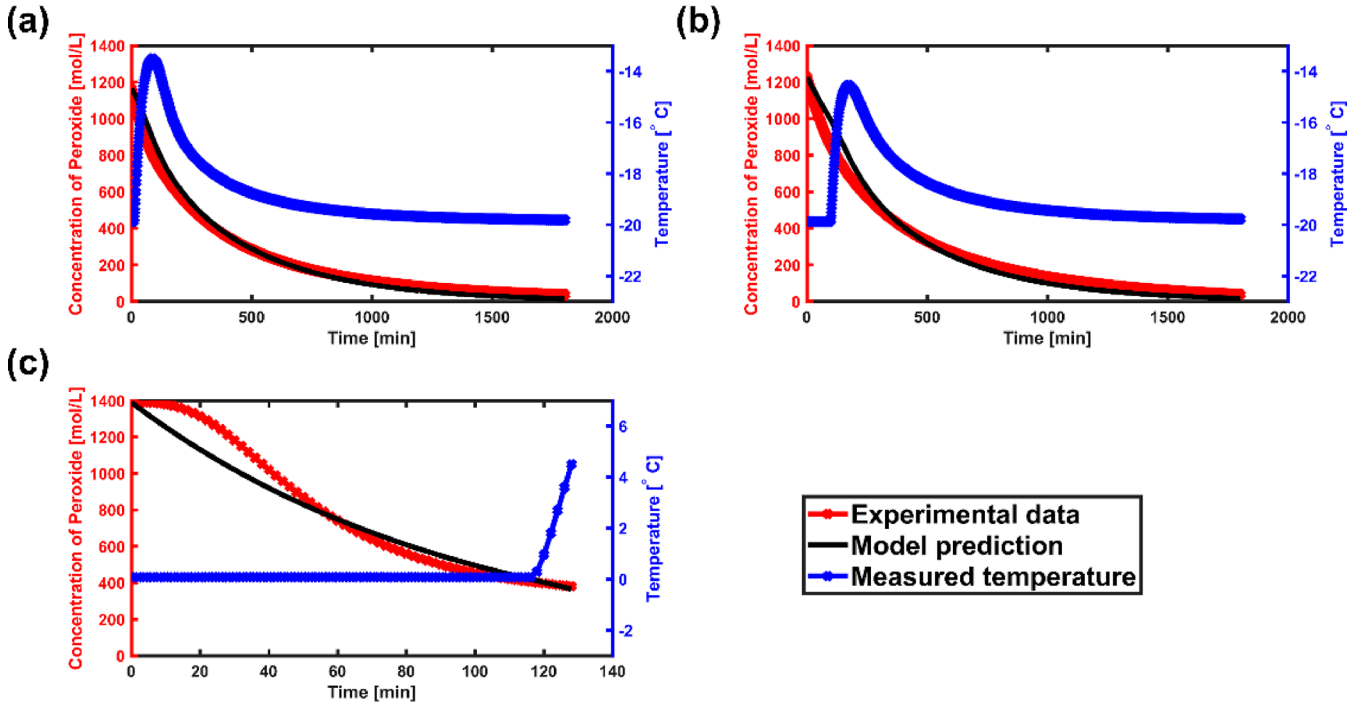

Figure 2. Comparison between model predictions and experimental data for the reaction shown in eq 3 (a) at −20 °C, (b) in a technical replicate of (a) to understand the batch-to-batch variability, and (c) at 0 °C to understand the impact of temperature. Also shown are the measured temperatures to demonstrate temperature control and the exothermic nature of the reaction. In (c), the data used for parameter estimation were cropped when the exotherm began (max spike ≈ 15 °C).

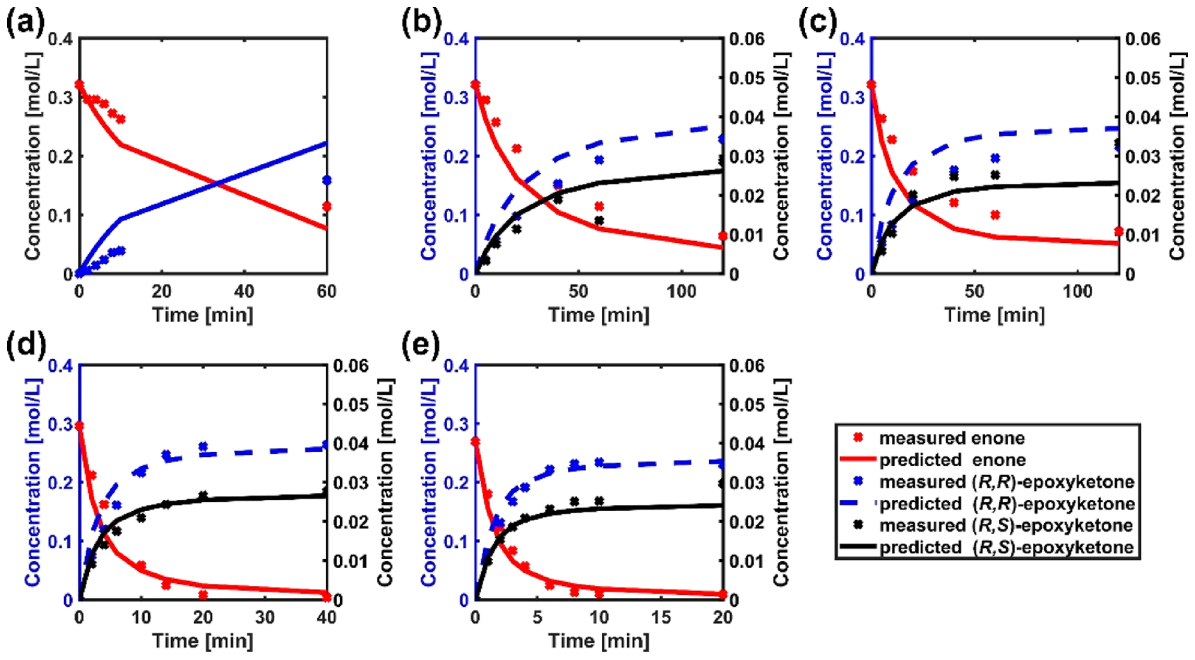

Figure 3. Comparison between experimental data and model predictions with inclusion of eq 3 for the enone, (*R*,*R*)-epoxy ketone, and (*R*,*S*)-epoxy ketone concentrations for reactions run at (a) −18 °C and 0.01 mol % catalyst, (b) −18 °C and 0.01 mol % catalyst, (c) −8 °C and 0.01 mol % catalyst, (d) −18 °C and 0.05 mol % catalyst, and (e) −18 °C and 0.1 mol % catalyst.

parameter estimation strategy is that the presence of the enone and epoxy ketone does not dramatically impact the kinetics of hydrogen peroxide decomposition. The conversions in CSTR2 and CSTR3 from the model with this assumption exhibit strong agreement with the experimental data in Figure 5.

Following batch characterization, the performances of the two models were compared for five different sets of reactions conditions performed in a continuous manner, in which the reaction temperature was held at −18 °C, the Mn catalyst loading was varied between 0.035 and 0.045 mol %, the number of equivalents of hydrogen peroxide was varied between 1 and 2, and each CSTR contained around 700 mL of total reaction mixture. The results are shown in Figure 4. This comparison highlights the importance of characterizing eq 3: without this

https://dx.doi.org/10.1021/acs.oprd.0c00189
Org. Process Res. Dev. 2020, 24, 1891−1908

Table 2. Regressed Kinetic Parameters of the Epoxidation Reaction with Hydrogen Peroxide Decomposition (T_{ref} = −20 °C)

reaction	rate constant $[(m^3/mol)^{n-1}\ s^{-1}]$	E_a (kJ/mol)
eq 1	$8.83 \times 10^{-5} \pm 3.1 \times 10^{-6}$	35.9 ± 3.4
eq 2	$9.43 \times 10^{-6} \pm 2.58 \times 10^{-7}$	29.7 ± 2.7
eq 3	$4.01 \times 10^{-3} \pm 1.08 \times 10^{-4}$	55.2 ± 3.5

characterization, the model overpredicts the conversion in CSTR2 in all cases and predicts that a different number of CSTRs is required to reach the desired 99% conversion. The model without eq 3 underpredicts the conversion in Figure 1 and overpredicts the conversions in Figure 4. This is consistent with the behaviors of stirred tanks and batch reactors when competing reactions (here eqs 1 and 2 versus eq 3) are involved.

Following this comparison, the model with eq 3 was used to determine a set of conditions where the enone conversion would surpass the desired conversion. The updated model led to increased understanding of the reaction conversion mechanism and the impact of H_2O_2 decomposition, which resulted in lower conversion of the desired reaction. The optimized process conditions to reach >99% conversion were determined to be 1.8 equiv of H_2O_2 fed to both CSTR1 and CSTR2 with a total of three CSTRs at a residence time of 15 min in each reactor, and process was designed accordingly. Splitting the H_2O_2 addition between two CSTRs is critical for reaching the desired conversion, as it reduces the exotherm and total H_2O_2 decomposition. This experiment began with reactors filled with ACN only. The predictions of the updated model were verified experimentally, as shown in Figure 5. The gas evolution observed in CSTR1 challenged a quantitative assessment of the reaction stream and rendered the concentration measurements more variable than those obtained in CSTR2 and CSTR3.

2.1.2. Workup Steps: Reaction Kinetics, Liquid–Liquid Extractions, Mass Transfer, and Model Development. Three reactions are considered in CSTR4: (1) the reaction of enone **1** with bisulfite (HSO_3^-) to form an enone sulfite adduct (eq 5),[25]

$$\text{enone} + HSO_3^- \rightarrow \text{enone sulfite adduct} \quad (5)$$

(2) the H_2O_2-catalyzed reaction of enone **1** with HSO_3^- to form the enone sulfite adduct (eq 6),

$$\text{enone} + HSO_3^- \xrightarrow{H_2O_2} \text{enone sulfite adduct} \quad (6)$$

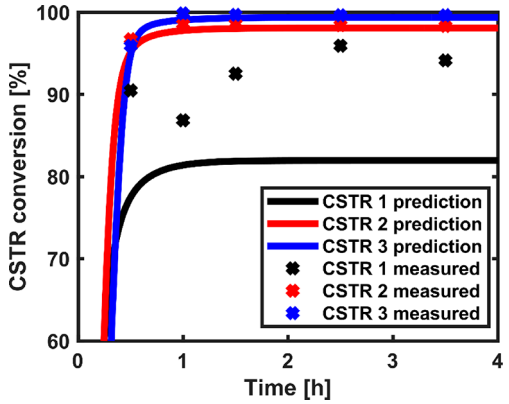

Figure 5. Comparison between model predictions and experimental data for the final validation of the H_2O_2-dependent reaction kinetic formulation. Experimentally, 1.8 equiv of H_2O_2 was fed to both CSTR1 and CSTR2, and a total of three CSTRs were used with a residence time of 15 min and a temperature of −15 °C for each reactor. All three CSTRs were initially filled with acetonitrile only.

and (3) the decomposition of hydrogen peroxide (eq 3). To characterize the reaction kinetics, a set of batch experiments with reaction temperatures between 30 and 50 °C and enone impurity between its nominal value and 3 times the nominal value was executed. The volumetric scale of the experiments was 2 to 3 mL of total reaction mixture, and time series data were collected in every reaction to track the depletion of the enone via HPLC, as shown in Figure 6. The mass transfer was studied for this reaction, and no mass transfer limitations were observed in the characterized stirring rate range of 350−950 rpm.

The reaction was modeled to follow first-order reaction kinetics with respect to all reactants, and the kinetic rate constants for the Arrhenius equation are provided in Table 3. To avoid overfitting, the activation energies for eqs 5 and 6 were assumed to be the same, and the temperature dependence of eq 3 was assumed to be negligible. The model accuracy could be improved by characterizing the hydrogen peroxide breakdown, similar to what was done for the productive reaction described above, but since 99% conversion was specified at the end of the productive reaction and this quench reaction does not directly correlate to a tight specification, this was not needed. The rate constant for eq 3 in CSTR4 is different from the rate constant for eq 3 in CSTR1, CSTR2, and CSTR3 as a result of many factors,

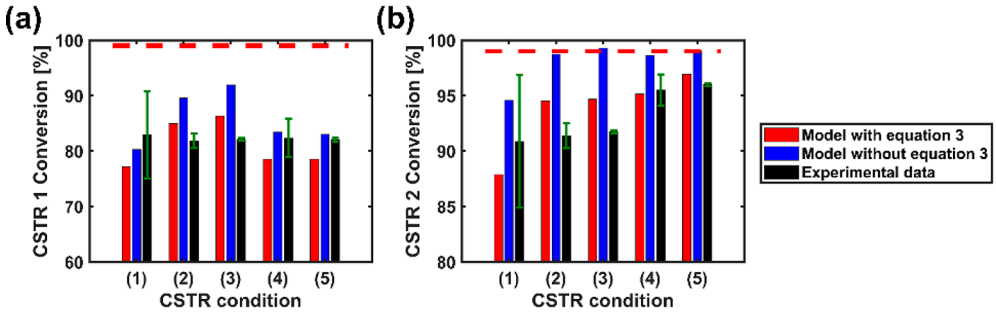

Figure 4. Comparison between model predictions for enone conversion in (a) CSTR1 and (b) CSTR2 with and without eq 3 under various sets of conditions: (1) 0.035 mol % catalyst with 1 equiv of hydrogen peroxide fed to CSTR1, (2) 0.035 mol % catalyst with 1.5 equiv of hydrogen peroxide fed to CSTR1, (3) 0.045 mol % catalyst with 1.4 equiv of hydrogen peroxide fed to CSTR1, (4) 0.045 mol % catalyst with 0.9 equiv of hydrogen peroxide fed to CSTR1 and 0.45 equiv of hydrogen peroxide fed to CSTR2, and (5) 0.045 mol % catalyst with 0.9 equiv of hydrogen peroxide fed to CSTR1 and 0.9 equiv of hydrogen peroxide fed to CSTR2.

https://dx.doi.org/10.1021/acs.oprd.0c00189
Org. Process Res. Dev. 2020, 24, 1891−1908

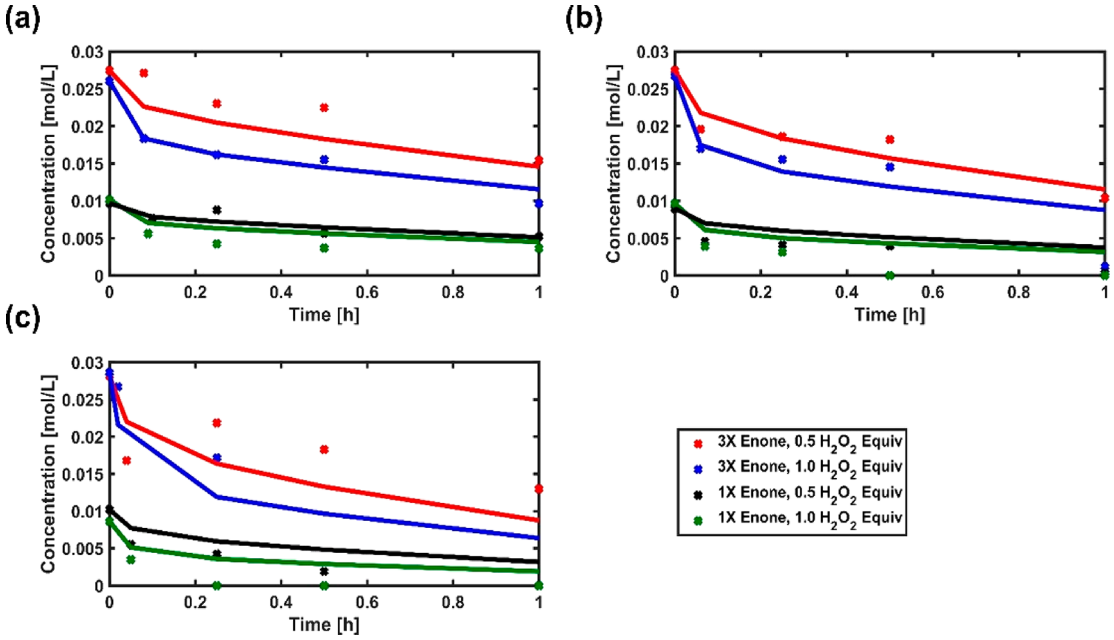

Figure 6. Comparison between model predictions and measurements for the breakdown of enone **1** in CSTR4 at (a) 30 °C, (b) 40 °C, and (c) 50 °C for various numbers of molar equivalents of hydrogen peroxide with respect to the enone feed for the epoxidation process and various enone impurity levels (1×, 3×) leaving the epoxidation process.

Table 3. Regressed Kinetic Parameters of the Quench Reaction (Classical Arrhenius)

reaction	rate constant $[(m^3/mol)^{n-1}\ s^{-1}]$	E_a (kJ/mol)
eq 5	$2.52 \times 10^{0} \pm 1.82 \times 10^{-1}$	25.0 ± 0.2
eq 6	$5.52 \times 10^{-2} \pm 1.86 \times 10^{-5}$	25.0 ± 0.2
eq 3	$2.19 \times 10^{-2} \pm 2.65 \times 10^{-4}$	–

including the reaction temperature and chemical species present.

Following these reactions, the biphasic stream undergoes a liquid−liquid phase separation in decanter 1 (DEC1). To characterize the phase separation and mass transfer kinetics between the aqueous and organic layers, batch experiments were designed and executed. These experiments aimed to characterize the impact of varying the process parameters, such as the enone conversion, the selectivity for the (*R*,*R*)-epoxy ketone over the (*R*,*S*)-epoxy ketone, and the solvent flow rates, on the process outcomes, such as the partitioning and mass transfer of impurities. In the experiments to characterize the equilibrium partition coefficients, the total solvent content was kept constant, and the compositions of AcOH, water, and ACN were varied up to ±15% of their nominal values. Additionally, the enone and (*R*,*S*)-epoxy ketone impurity levels were increased up to 3 times their nominal values, while the (*R*,*R*)-epoxy ketone concentration was kept at its nominal amount and the temperature was varied, as summarized in Table 4.

To ensure that the phases reached equilibrium, the liquid−liquid extraction was carried out for 24 h before analysis of both phases for the contents of the enone, (*R*,*R*)-epoxy ketone, and (*R*,*S*)-epoxy ketone by UPLC, ACN and AcOH by GC, and water by Karl Fisher (KF) titration. The extraction was modeled using the partition coefficient, i.e., the ratio of the concentration of a species in the organic phase divided by the concentration of that same spaces in the aqueous phase. The partition coefficients (H) for the (*R*,*R*)-epoxy ketone, the (*R*,*S*)-epoxy ketone, and water were found to depend on the reaction temperature (T),

Table 4. Design of Experiments for Characterization of Liquid−liquid Extraction 1[a]

		compound concentration(mg/mL)			solvent vol %		
expt	T (°C)	(*R*,*R*)- epoxy ketone (P)	enone (I1)	(*R*,*S*)- epoxy ketone (I2)	water	ACN	AcOH
1	T_1	1×	3×	3×	N	N	N
2		1×	3×	3×	N + 15%	R	R
3		1×	3×	3×	N − 15%	R	R
4		1×	3×	3×	R	N + 15%	R
5		1×	3×	3×	R	N − 15%	R
6		1×	1×	1×	N	N	N
7	T_2	1×	3×	3×	N	N	N
8		1×	3×	3×	N + 15%	R	R
9		1×	3×	3×	N − 15%	R	R
10		1×	3×	3×	R	N + 15%	R
11		1×	3×	3×	R	N − 15%	R

[a]Abbreviations: N, nominal; R, residual (from 100 vol %); 1×, nominal concentration; 3×, 3 times the elevated impurity concentration.

https://dx.doi.org/10.1021/acs.oprd.0c00189
Org. Process Res. Dev. 2020, 24, 1891−1908

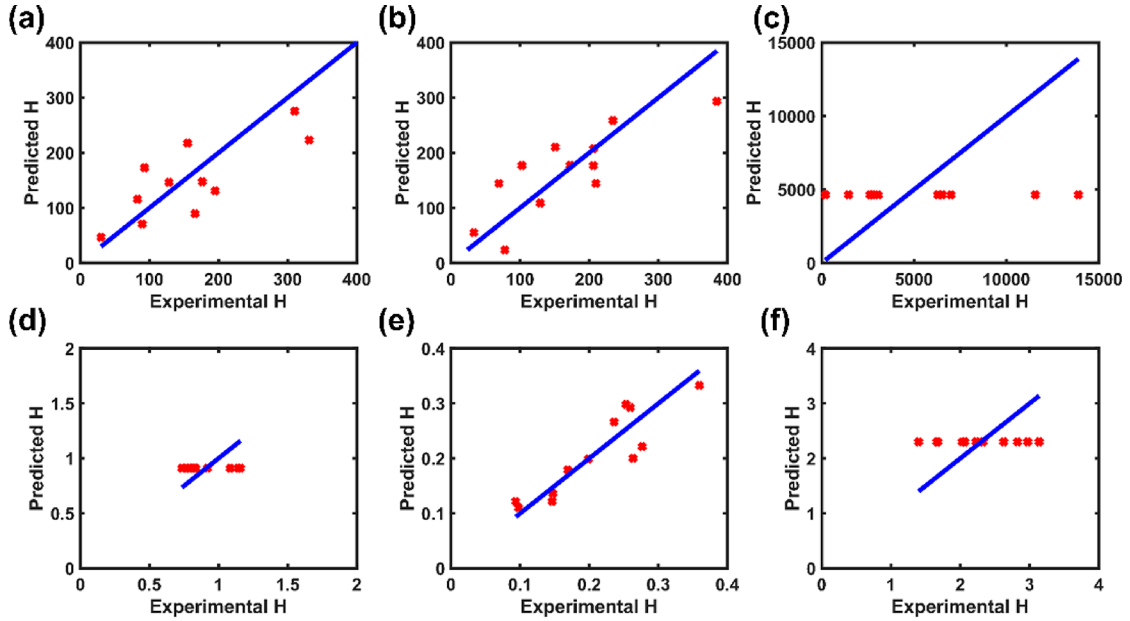

Figure 7. Comparison between the measured and regressed partition coefficients (H) in CSTR4 for (a) the (R,R)-epoxy ketone, (b) the (R,S)-epoxy ketone, (c) the enone, (d) acetic acid, (e) water, and (f) acetonitrile.

water content ($w_{water,tot}$), and ACN content ($w_{ACN,tot}$), as shown in eq 7:

$$\ln H = \frac{a}{T} + bw_{water,tot} + cw_{ACN,tot} + d \tag{7}$$

in which the parameters a, b, c, and d were obtained via least-squares minimization. Figure 7 shows these correlations as well as the lack of correlation for the partition coefficients of acetic acid, acetonitrile, and enone. Therefore, the partition coefficients of the latter species were modeled as the average values of the experimental observations. The regressed parameters for these data are given in Table 5.

Table 5. Regressed Parameters of Equation 7 for the Partition Coefficients of Species in CSTR4 Along with R^2 Values Describing the Goodness of the Fits

component	a	b	c	d	R^2
(R,R)-epoxy ketone	−1820	21.8	9.61	−2.69	0.71
(R,S)-epoxy ketone	297	28.0	17.3	−14.7	0.65
enone	0	0	0	8.44	–
AcOH	0	0	0	−0.094	–
water	−472	5.74	15.8	−6.49	0.84
ACN	0	0	0	0.833	–

At a reactor size of 100 mL, a temperature of 40 °C, and a stirring rate of 400 rpm, the time required for mass transfer of all species (solvents, solutes, and water) in this step was experimentally confirmed to be much shorter (on the order of <5 min) than the process time scale (40 min) (Figure 8). Therefore, fast mass transfer kinetics was assumed for all of the solutes and liquid species, and the models were implemented under the assumption that the phase partitioning follows the equilibrium partition coefficients at all times.

2.2.3. MSMPR Crystallization and Model Development. Following liquid−liquid extraction, the organic fraction leaving DEC1 is sent to a two-stage MSMPR crystallization cascade for cooling and antisolvent (water) crystallization. In MSMPR1, the process stream, water, acetic acid, and acetonitrile are supplied for crystallization. To improve the recovery of the (R,R)-epoxy ketone, the slurry leaving MSMPR1 is fed to MSMPR2, which operates at a lower temperature. This decreases the solubility of the (R,R)-epoxy ketone in MSMPR2 while suppressing the formation of fine crystals and secondary nucleation in MSMPR1. The solubility data for the (R,R)-epoxy ketone were observed to follow a van't Hoff relationship, where the effect of the solvent composition can be attributed entirely to a linear variation of the entropy term (the intercept of the logarithmic solubility function) in the Gibbs free energy of the dissolution process (Figure 9a,b). Accordingly, the van't Hoff solubility expression was modified to include solvent effects as shown in eq 8:

$$\ln x = -\frac{A}{T} + Bv_{antisolvent} + C \tag{8}$$

where x is the solubility, T is the absolute temperature, and $v_{antisolvent}$ is the volume fraction of antisolvent in the solute-free solvent system. The values of the parameters A, B, and C obtained by regression are given in Table 6.

To obtain experimental solubility and equilibrium distribution coefficient data, a set of batch and continuous experiments at reaction temperatures between 5 and 25 °C, enone impurity levels between the nominal value and 3 times the nominal value, water volume fractions from 0.65 to 0.8, ACN volume fractions from 0.1 to 0.175, and AcOH volume fractions from 0.1 to 0.175 were designed and executed. In the batch experiments, the total crystallization mixture volume was ∼1 mL. After addition of the antisolvent, the samples were allowed to crystallize at constant temperature for 24 h. Subsequent filtration using a 0.2 μm syringe filter followed by HPLC analysis of the liquid phase was employed to calculate the system solubility at each temperature and solvent composition. Equilibrium distribution coefficients were calculated on the basis of the HPLC data from the feed and mother liquor combined with the mass balance for the system. End-point data were collected via HPLC to determine the solubility of the (R,R)-epoxy ketone, as shown in Figure 9.

https://dx.doi.org/10.1021/acs.oprd.0c00189
Org. Process Res. Dev. 2020, 24, 1891−1908

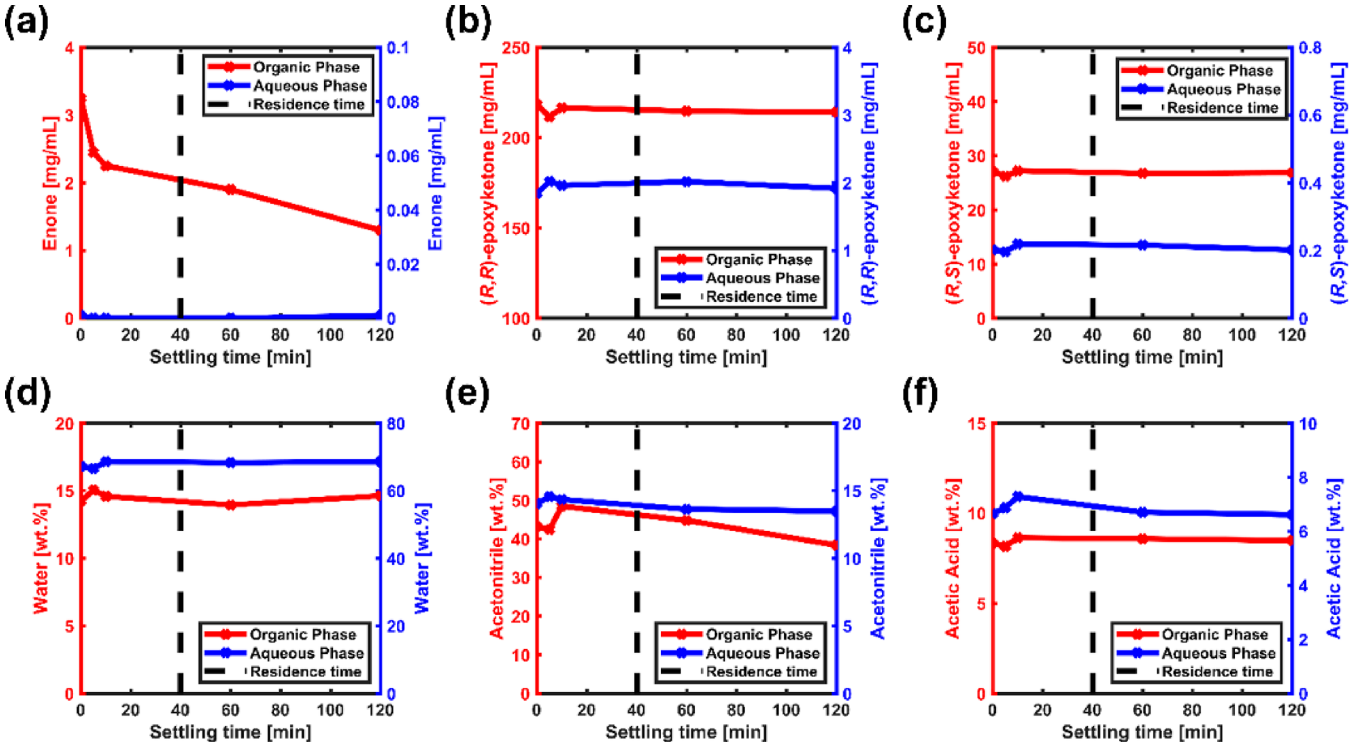

Figure 8. Determination of the mass transfer rates in CSTR4 for (a) the enone, (b) the (*R*,*R*)-epoxy ketone, (c) the (*R*,*S*)-epoxy ketone, (d) water, (e) acetonitrile, and (f) acetic acid. A data set was generated at 500 rpm and demonstrated a negligible impact on the agitation rate.

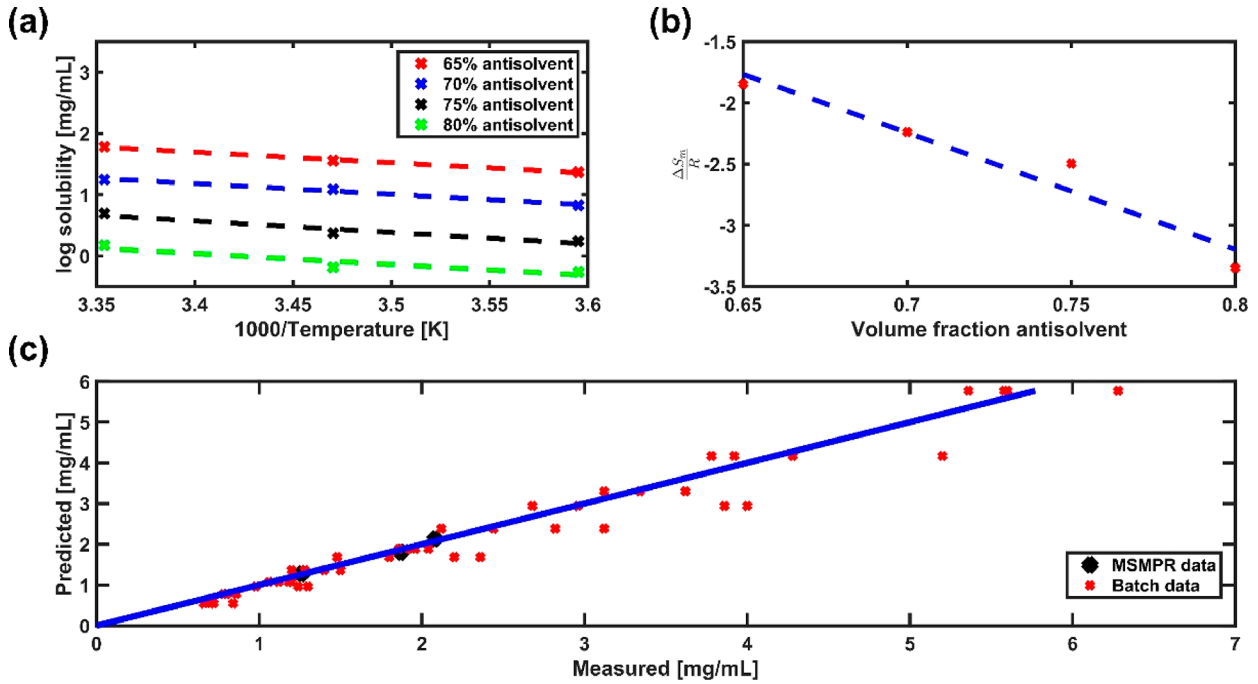

Figure 9. (a) Demonstration of the van't Hoff dependence of the (*R*,*R*)-epoxy ketone solubility at varying antisolvent (AS) compositions. (b) Demonstration of linear variation of the entropy term for the solubility of the (*R*,*R*)-epoxy ketone. (c) Comparison between measured and regressed solubilities (in mg/mL) of the (*R*,*R*)-epoxy ketone for various conditions.

Continuous MSMPR crystallization experiments were used to determine the crystal growth rate (G) and nucleation rate (B) from steady-state data. The experimental setup was built around a Mettler Toledo EasyMax reactor system, including two MSMPR crystallizers in series, each equipped with a 45° downpumping impeller (50 mm diameter, 600 rpm), and having an operating volume of 80 mL. The transfer of feed and antisolvent was conducted in a continuous manner using syringe pumps. To avoid segregation of solids, product withdrawal was conducted intermittently by removing 10% of the crystallizer volume every 10% of the residence time and controlling the vessel volume by means of a dip pipe.[26] This withdrawal was

https://dx.doi.org/10.1021/acs.oprd.0c00189
Org. Process Res. Dev. 2020, 24, 1891−1908

Table 6. Van't Hoff Solubility Model Parameters for the Solubility of the (*R*,*R*)-Epoxy Ketone in a Mixture of Acetic Acid, Water, and Acetonitrile

parameter	value	units
A	2.79×10^3	K
B	−12.0	–
C	9.58	–

conducted using programmable peristaltic pumps operating at full speed. The onset of the steady state was determined in situ via focused beam reflectance measurement (FBRM) and infrared (IR) spectroscopy and later verified via HPLC analysis of the mother liquor. Mother liquor samples were taken every residence time via syringe filtration (0.2 μm filter) of the MSMPR suspension. In addition, a consistent crystal habit was verified via optical microscopy analysis of the crystallization slurry, and a consistent solvent composition was verified via KF titration of the mother liquor. The outlet of the crystallization setup was directed to a vacuum filtration setup to collect the solid material. This material was analyzed via HPLC and X-ray powder diffraction (XRPD) to quantify the impurity incorporation and verify a consistent crystal morphology, respectively. By means of this data-rich methodology, transient and steady-state information could be obtained for the crystal chord length distribution, crystal habit, crystal structure, solvent composition, and impurity distribution coefficients.

The residence time was maintained constant between the two stages, with the entire antisolvent addition being conducted in the first stage. Across experiments, the operating residence times varied between 30 and 45 min, and the temperature was varied between 10 and 20 °C in the first stage and between 5 and 10 °C in the second stage. To simplify parameter estimation, the antisolvent (water) concentration was maintained constant at 72.5 vol %. The crystallization kinetics was modeled using semiempirical rate equations (eqs 9 and 10)

$$G = k_{g0} \exp\left(\frac{-E_{ag}}{RT}\right)\sigma \tag{9}$$

$$B = k_{b0} \exp\left(\frac{-E_{ab}}{RT}\right)\sigma^2 M_T^{2/3} \tag{10}$$

where the the supersaturation orders for nucleation and growth were assumed to be 2 and 1, respectively. These rate equations are functions of a pre-exponential factor (k_{g0} or k_{b0}) as well as an activation energy for nucleation (E_{ab}) or growth (E_{ag}). While the effects of process parameters such as the supersaturation (σ) and suspension density (M_T) are directly quantified, the effects of mixing and solvent composition are lumped into the pre-exponential factor. In this case, the supersaturation is calculated from its thermodynamic definition as a function of the mole fractions under saturated (x_{sat}) and supersaturated (x) conditions, assuming an activity coefficient ratio of 1 (eq 11):

$$\sigma = \ln \frac{x}{x_{sat}} \tag{11}$$

The kinetic parameters were regressed from steady-state data by means of the method of moments for an ideal MSMPR crystallizer[27] in combination with the crystallizer mass balance using the square-weighted mean chord length and the mother liquor concentration as the objective variables, as explained in similar work.[28] Because all of the experiments presented similar crystal aspect ratios and the same crystal structure, a single set of parameters was regressed from the unidimensional chord length distribution data. The presence of loosely bound aggregates hindered the chord length distribution data, often presenting a bimodal distribution in return. Because of the significant size difference, it was possible to employ only the first peak (free-flowing single crystals) for model calibration. These aggregates do not survive the washing process, and the particle size distribution is not a critical parameter for this intermediate. Hence, this simplification was applied instead of modeling the

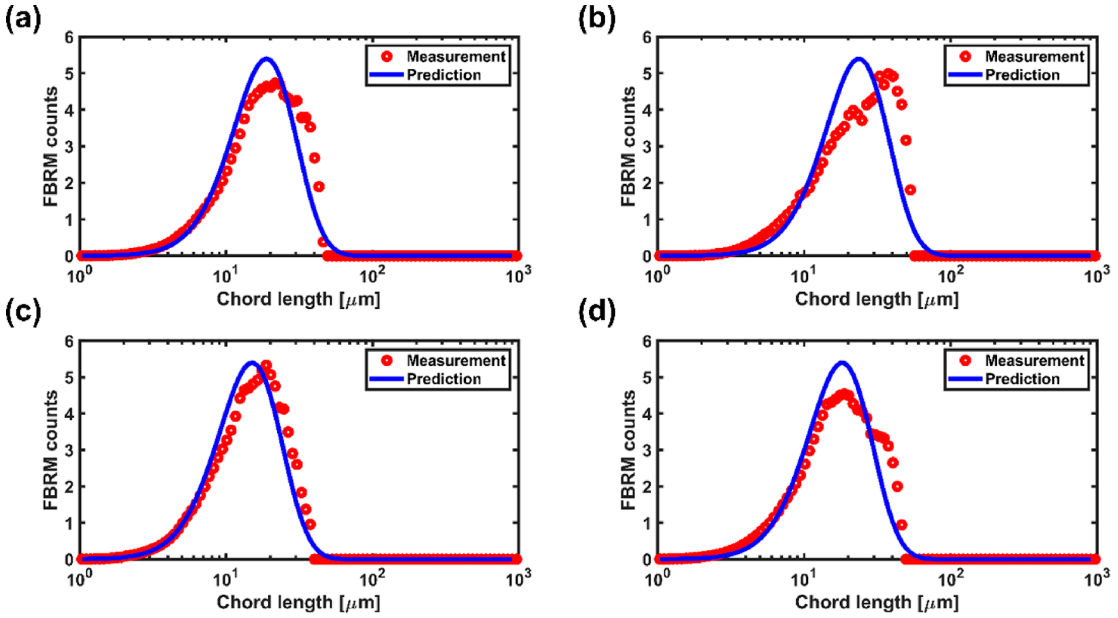

Figure 10. Comparison between model predictions and measured FBRM square-weighted counts for continuous MSMPR crystallization at (a) 20 °C with a 30 min residence time, (b) 10 °C with a 30 min residence time, (c) 20 °C with a 45 min residence time, and (d) 15 °C with a 30 min residence time. These data are from the first MSMPR stage of each experiment, used for calibration of the crystallization kinetics.

https://dx.doi.org/10.1021/acs.oprd.0c00189
Org. Process Res. Dev. 2020, 24, 1891−1908

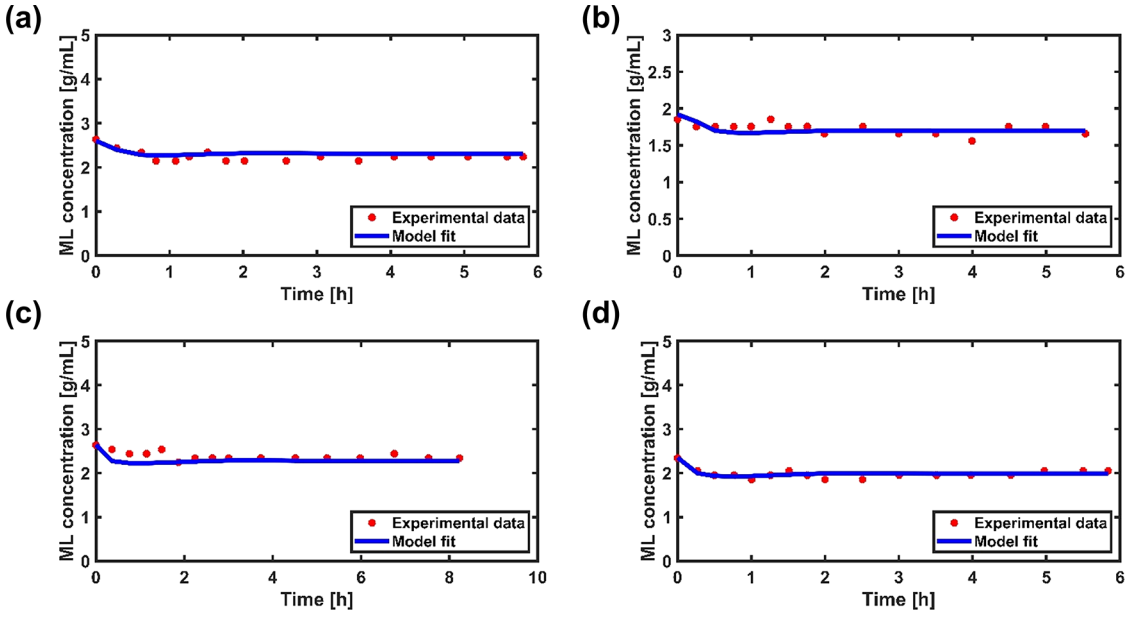

Figure 11. Comparison between model predictions and measured mother liquor concentrations for continuous MSMPR crystallization at (a) 20 °C with a 30 min residence time, (b) 10 °C with a 30 min residence time, (c) 20 °C with a 45 min residence time, and (d) 15 °C with a 30 min residence time. These data are from the first MSMPR stage of each experiment, used for calibration of the crystallization kinetics.

aggregation process, and the accuracy of the model for prediction of the yield and chiral purity was validated separately. Comparisons between the experimental data and model fits are shown in Figures 10 and Figure 11, and the kinetic parameter estimates are given in Table 7.

Table 7. Parameter Estimates for the Crystallization Process

Crystallization Kinetics		
parameter	value	units
k_{b0}	1.75×10^{10}	$g^{-1}\ s^{-1}$
E_{ab}	25.13	kJ/mol
k_{g0}	3.75	μm/s
E_{ag}	12.35	kJ/mol
Distribution Coefficient (All Unitless)		
parameter	enone	(*R*,*S*)-epoxy ketone
$\alpha_{batch,1\times imp}$	−15.38	−0.17
$\beta_{batch,1\times imp}$	0.78	0.12
$\alpha_{batch,3\times imp}$	−15.66	−0.38
$\beta_{batch,3\times imp}$	1.41	0.36
α_{MSMPR}	−16.87	−0.064
β_{MSMPR}	1.19	0.047

Finally, incorporation of the impurity (the enone or (*R*,*S*)-epoxy ketone) into the (*R*,*R*)-epoxy ketone crystals was taken into account using a distribution coefficient model, as shown in eq 12:[29]

$$DC_i = \frac{M_{T,i}/M_{T,solute}}{C_{ml,i}/C_{ml,solute}} = \alpha_i \frac{C_{ml,i}}{C_{ml,i} + C_{ml,solute}} + \beta_i \quad (12)$$

Here the impurity distribution coefficient (DC_i) is defined as the ratio of the relative concentrations of solute and impurity in the solid phase ($M_{T,solute}$ and $M_{T,i}$, respectively) divided by the ratio of relative concentrations in the liquid phase ($C_{ml,solute}$ and $C_{ml,i}$). These can be predicted from mother liquor concentration data[30] using α_i and β_i as parameters that depend on the solvent composition, temperature, crystal form, and concentration of foreign species.

Both the batch and continuous data were used, as shown in Figure 12, and the parameter estimates are shown in Table 7. As the distribution coefficients varied among the crystallization conditions, the data from the continuous experiment were used in the full simulation, as they match the levels of supersaturation and suspension density expected at scale. Finally, because each stage operates at different supersaturations, the product will have different impurity concentrations across the crystal lattice. Thus, the final crystal chiral purity was calculated on the basis of the mass deposition and the distribution coefficient in each crystallization stage, accounting for the history of the crystalline phase.

2.2.4. Filtration Device and Model Development. The final operations in this manufacturing process are filtration, washing of the collected cake, and dissolution of the solids in the slurry removed from MSMPR2. Two parallel batch filtration units are used to allow for continuous production of the product solution. The filter model is based on modified Darcy's law (eqs 13 and 14):[31,32]

$$\frac{t}{m} = \frac{\mu}{A\Delta P}\left(\frac{m_s}{Cm}\right)\left(\frac{\alpha}{2}\frac{m_s}{A} + R_m\right) \quad (13)$$

$$\alpha = \alpha_0\left(\frac{\Delta P}{\Delta P_{ref}}\right)^n \quad (14)$$

where m_s is the mass of solids, μ is the filtrate viscosity, α is the specific cake resistance (length/mass), A is the filtration area, R_m is the medium resistance, t is the filtration time, ΔP is the pressure drop across the cake, m is the mass of the filtrate, C is the mass of solids per unit volume of liquid in the slurry, ρ is the filtrate density, and n is the cake compressibility. This model was modified to account for continuous operation at constant ΔP, as shown in eq 15:

https://dx.doi.org/10.1021/acs.oprd.0c00189
Org. Process Res. Dev. 2020, 24, 1891−1908

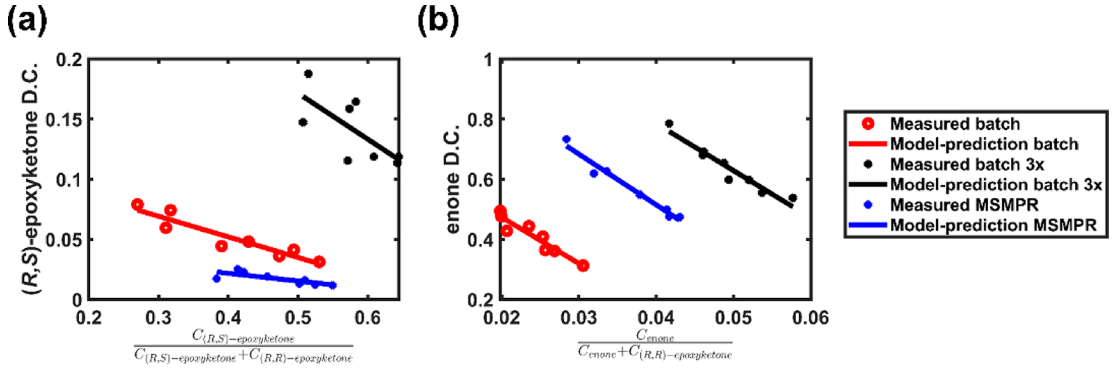

Figure 12. Comparison between measured and regressed distribution coefficients of (a) the (*R*,*S*)-epoxy ketone and (b) the enone for the batch crystallization at the nominal impurity level (red), the batch crystallization at 3 times the nominal impurity level (blue), and continuous crystallization at the nominal impurity level (black).

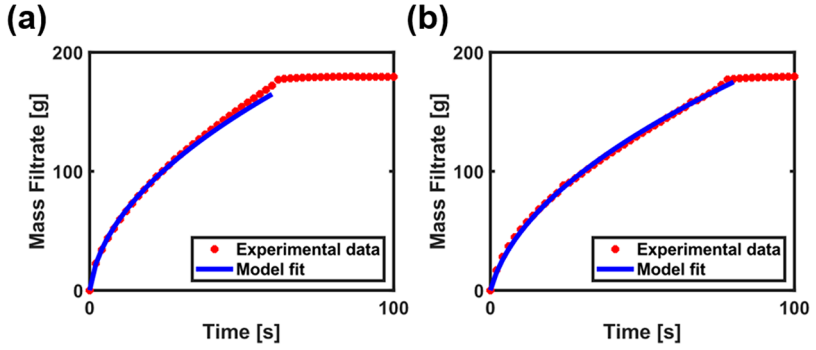

Figure 13. Comparison between model predictions and experimental data for filtration at (a) 26 psi and (b) 12.5 psi.

$$\frac{dm}{dt} = \left[\left(\frac{\mu R_m}{\rho A \Delta P}\right)^2 + 4\left(\frac{\mu \alpha \frac{m_s}{m}}{\rho 2A^2 \Delta P}\right)t\right]^{-1/2} \quad (15)$$

A set of two experiments were designed and executed in which ΔP was varied from 12.6 to 25 psi and the mass of the filtrate over time was recorded, as shown in Figure 13. The determined kinetic parameters are shown in Table 8. The cake resistance α was $<1 \times 10^{10}$ m/kg and the compressibility n was <1, which suggested[32] that the cake is uncompressible under the operating conditions and confirmed that the operation is suitable for vacuum/pressure filtration. Short filtration times were achieved, and no particle compression or breakage was observed.

Table 8. Parameter Estimates for the Filtration Process

parameter	description	value	units
α_0	cake resistance	$(9.47 \pm 0.05) \times 10^9$	m/kg
n	cake compressibility	0.922 ± 0.004	–
R_m	medium resistance	$(1.40 \pm 0.02) \times 10^8$	cm^{-1}

Furthermore, as heptane is used for one of the wash steps, the solubility of the (*R*,*R*)-epoxy ketone was modeled using a van't Hoff relationship as shown in eq 8, but without an antisolvent dependence. To determine the model parameters, a set of experiments with temperatures from −5 to 25 °C were conducted, as shown in Figure 14, and the model parameters can be found in Table 9. There is some experimental variability in Figure 14 because the solubility in heptane is low. Again, this level of model uncertainty is allowable, as the amount of (*R*,*R*)-epoxy ketone dissolution in heptane does not directly correlate to an impurity specification and is negligible compared with the total amount of solid.

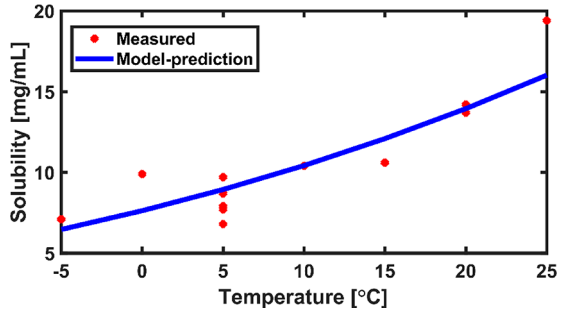

Figure 14. Comparison between measurements and the van't Hoff fit for the solubility of the (*R*,*R*)-epoxy ketone in heptane.

Table 9. Van't Hoff Solubility Model Parameters for the Solubility of the (*R*,*R*)-Epoxy Ketone in Heptane

parameter	value	units
A	2.42×10^3	K
C	10.9	–

2.3. Computational Methods. The end-to-end simulation was created in gPROMS FormulatedProducts version 1.2.2 fronm Process Systems Enterprise.[33] A database containing physical and thermodynamic properties of proprietary and other compounds was developed using gPROMS FormulatedProducts Utilities and MultiFlash 6.1. All of the CSTRs and decanters were modeled with the gPROMS FormulatedProducts standard and custom library models. The MSMPRs and filters were modeled using custom-built code and relevant equations.

https://dx.doi.org/10.1021/acs.oprd.0c00189
Org. Process Res. Dev. 2020, 24, 1891−1908

Kinetic parameter estimates for the reactions occurring in CSTR1, CSTR2, and CSTR3 were determined in MATLAB[34] using concentration and temperature measurements for both the reactant and product. The reactions occurring in CSTR4 were estimated in gPROMS FormulatedProducts version 1.2.2 using concentration measurements for the reactant. Partition coefficients for the liquid−liquid equilibrium in DEC1 had a dependence on temperature, water fraction, and acetonitrile fraction and were modeled as such. The mass transfer coefficients for the liquid−liquid equilibrium in DEC1 were confirmed to be sufficiently large and were not estimated. For MSMPR1 and MSMPR2, aggregates were observed in the FBRM as a bimodal distribution. The unweighted chord length distribution measurements were manually curated in Microsoft Excel to truncate the aggregate distribution, giving a unimodal distribution of free-flowing crystals that followed the assumptions of an ideal MSMPR crystallizer. The crystallization parameters were determined in gPROMS FormulatedProducts version 1.2.2 (kinetics) and in Microsoft Excel using linear regression (solubility and distribution coefficients). Finally, the filtration parameters were determined in gPROMS Formulated Products version 1.2.2.

For level control within each relevant unit operation, the outflow condition was based on a fixed-volume specification. For temperature control, an embedded model was used to manipulate the temperature of the incoming heat transfer fluid. Heat transfer coefficients for glass reactors were estimated to be 4.56 W/K using DynoChem Utilities.[35]

For disturbance analysis, the simulation was run with nominal conditions to reach the steady state (10 000 s), unless otherwise specified. Following this, disturbances were introduced as step changes and allowed to run to steady state. Process disturbances were determined on the basis of the expected fluctuations at scale, and model disturbances were determined on the basis of either (1) the standard deviation of the determined parameters or (2) the largest difference between the model predictions and experimental data in the calibration set.

3. RESULTS AND DISCUSSION

After models for the individual unit operations were developed, the models were connected in a flowsheet-level integrated model including lower-level control loops (i.e., temperature, level, and flow rate) for dynamic simulation. The simulation was then used to perform disturbance analysis in order to determine how disturbances would impact downstream unit operation, especially the critical quality attributes (CQAs). The simulations allowed the determination of the process parameters (PPs) with the most impact on the CQAs and guided the development of a process control strategy to control those CQAs through manipulation of PPs. The target-level process specifications were initially developed for the batch process and were targeted by the continuous process. The uncertainties belong to two distinct groups. Process uncertainties in the form of operational disturbances include disturbances in the flow rate and composition of the feed stream, the temperature, and the fill level in every unit operation. The operational disturbances along with the allowed tolerances (relative to the nominal values) are shown in Table 10. Model uncertainties include parametric uncertainties of the estimated kinetic and thermodynamic parameters. The model uncertainties along with the allowed tolerance for each parameter are shown in Table 11. All of the process parameters were recorded in the simulation, but the major focus of this analysis is the conversion of the enone leaving CSTR3 and the chiral purity of the (*R*,*R*)-epoxy ketone crystals, both of which are CQAs.

Table 10. Process Uncertainties in the Form of Operational Disturbances Considered in the Disturbance Analyses

stream/unit operation	variable	allowed tolerance
enone solution in ACN/AcOH	flow rate	±10% of total flow rate
enone solution in ACN/AcOH	molarity of the enone	±10% of total molarity
Mn catalyst solution in ACN	flow rate	±10% of total flow rate
Mn catalyst solution in ACN	molarity of Mn	±10% of total molarity
50 wt % H_2O_2 in water	flow rate	±10% of total flow rate
50 wt % H_2O_2 in water	weight fraction of H_2O_2	±10% of total weight fraction
15 wt % aqueous sodium bisulfite	flow rate	±10% of total flow rate
15 wt % aqueous sodium bisulfite	weight fraction of $NaHSO_3$	±10% of total weight fraction
AcOH	flow rate	±10% of total flow rate
water	flow rate	±10% of total flow rate
ACN/AcOH/water wash solution	amount charged	±10% of amount charged
heptane wash	amount charged	±10% of amount charged
CSTR1	temperature	±5 °C
CSTR1	fill level	±10% of the reactor volume
CSTR2	temperature	±5 °C
CSTR2	fill level	±10% of reactor volume
CSTR3	temperature	±5 °C
CSTR3	fill level	±10% of reactor volume
MSMPR1	temperature	±5 °C
MSMPR1	fill level	±10% of reactor volume
MSMPR2	temperature	±5 °C
MSMPR2	fill level	±10% of reactor volume
MTBE dissolution solvent	amount charged	±10% of amount charged

Conversion of Enone Leaving CSTR3. The step response matrices for the conversion of the enone leaving CSTR3 are shown in Figure 15. For each parameter, a disturbance within predefined allowed tolerances was applied at four levels: nominal plus the maximum tolerance, nominal plus half the maximum tolerance, nominal minus half the maximum tolerance, and nominal minus the maximum tolerance. As shown, operational disturbances in the enone flow rate, enone concentration, hydrogen peroxide flow rate and concentration, and CSTR2 temperature have a greater impact on conversion. Additionally, the conversion is relatively sensitive to kinetic parameter estimates for the main conversion reaction as well as the hydrogen peroxide reaction. Furthermore, operational disturbances in the Mn catalyst concentration demonstrate a slight to negligible impact on the conversion, and all of the other disturbances and uncertainties have negligible impacts on the conversion in CSTR3 and are not shown.

The relative ordering of the impacts of these disturbances and uncertainties in one parameter at a time is shown in Figure 16. The large impacts of hydrogen peroxide and the enone are consistent with the fact that since they are the primary reactants, any changes in their concentrations should change the total

https://dx.doi.org/10.1021/acs.oprd.0c00189
Org. Process Res. Dev. 2020, 24, 1891−1908

Table 11. Model Uncertainties in the Form of Parametric Uncertainties Considered in the Disturbance Analyses

stream/unit operation	variable	allowed tolerance
CSTR1/CSTR2/CSTR3	pre-exponential factor for eq 1	±10% of absolute value
CSTR1/CSTR2/CSTR3	pre-exponential factor for eq 2	±10% of absolute value
CSTR1/CSTR2/CSTR3	pre-exponential factor for eq 3	±10% of absolute value
CSTR4	pre-exponential factor for eq 5	±10% of absolute value
CSTR4	pre-exponential factor for eq 6	±10% of absolute value
CSTR4	pre-exponential factor for eq 3	±10% of absolute value
CSTR4	(*R*,*R*)-epoxy ketone partition coefficient	+90/−50% of absolute value
CSTR4	(*R*,*S*)-epoxy ketone partition coefficient	+108/−70% of absolute value
CSTR4	enone partition coefficient	+2500/−70% of absolute value
CSTR4	water partition coefficient	±30% of absolute value
CSTR4	ACN partition coefficient	+70/−30% of absolute value
CSTR4	AcOH partition coefficient	±25% of absolute value
MSMPR1/MSMPR2	(*R*,*S*)-epoxy ketone distribution coefficient	±10% of absolute value
MSMPR1/MSMPR2	nucleation rate	±10% of absolute value
MSMPR1/MSMPR2	growth rate	±10% of absolute value

reaction rate. The Mn catalyst participates in both beneficial (eqs 1 and 2) and detrimental (eq 3) reactions for conversion of the enone. This explains the apparent lack of dependence on the Mn catalyst concentration and flow rate; increasing the amount of catalyst increases the rates of all of the reactions, but the impact is small because the reactions are competitive. This phenomenon helps explain the same effect for the fill levels of CSTR1, CSTR2, and CSTR3—increasing the total reaction rate for each species early in the process serves only to decompose hydrogen peroxide further. The effects of the CSTR1, CSTR2, and CSTR3 temperatures are more nuanced. Specifically, a temperature dependence of the conversion would be expected on the basis of the difference in the activation energies of the primary reactions. For example, decreasing the temperature should increase the overall conversion because of an increase in selectivity between enone conversion and hydrogen peroxide decomposition; however, this effect is minimized in CSTR1 because of the hydrogen peroxide stream entering CSTR2. The reason that this effect is not strongly observed in CSTR3 is is the very low concentration of reactants entering CSTR3 (98.5% conversion of the enone). Finally, the sensitivity of the conversion to the primary conversion rate constant and the hydrogen peroxide rate constant is consistent with fast competitive kinetics and demonstrates the value of the data generated in the reaction kinetics characterization studies, as demonstrated in Figures 4 and 5.

In terms of developing a more robust process, the worst-case combination of all disturbances was analyzed (Figure 17). This involved taking the condition for each letter in Figure 16 that resulted in the smallest (*R*,*R*)-epoxy ketone conversion. These disturbances were then combined to see the total impact on the (*R*,*R*)-epoxy ketone conversion: ∼98.5% conversion of the enone was maintained with the worst-case combination of all disturbances. This is close to the desired conversion of 99.0%, and further conversion of the enone in CSTR4 could result in a high-quality product. However, the conversion benefit obtained in CSTR3 from 98.5 to 99.5% overall conversion at steady state does suggest diminishing returns on adding another CSTR in

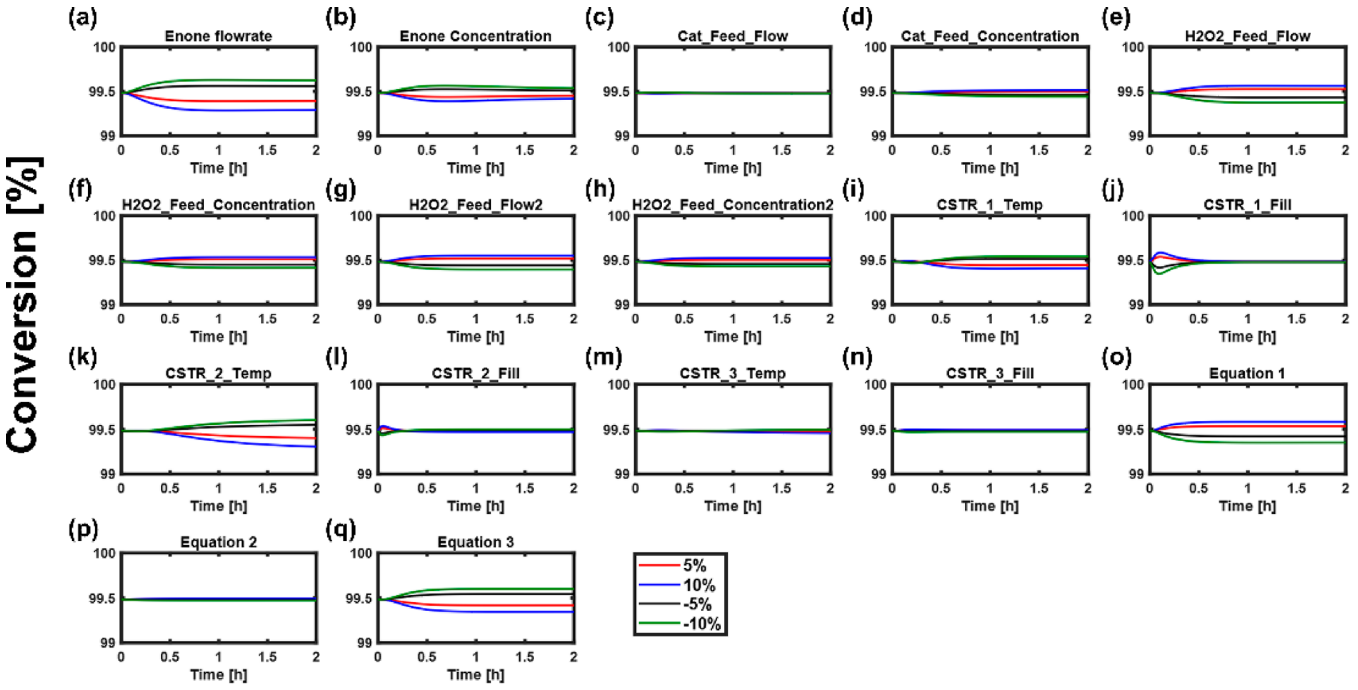

Figure 15. Conversion of the enone leaving CSTR3 as a function of each parameter individually: (a) enone flow rate, (b) enone concentration, (c) Mn catalyst flow rate, (d) Mn catalyst concentration, (e) flow rate of the hydrogen peroxide stream entering CSTR1, (f) concentration of the hydrogen peroxide stream entering CSTR2, (g) flow rate of the hydrogen peroxide stream entering CSTR2, (h) concentration of the hydrogen peroxide stream entering CSTR2, (i) CSTR1 temperature, (j) CSTR1 fill level, (k) CSTR2 temperature, (l) CSTR2 fill level, (m) CSTR3 temperature, (n) CSTR3 fill level, (o) pre-exponential factor for eq 1, (p) pre-exponential factor for eq 2, and (q) pre-exponential factor for eq 3.

https://dx.doi.org/10.1021/acs.oprd.0c00189
Org. Process Res. Dev. 2020, 24, 1891−1908

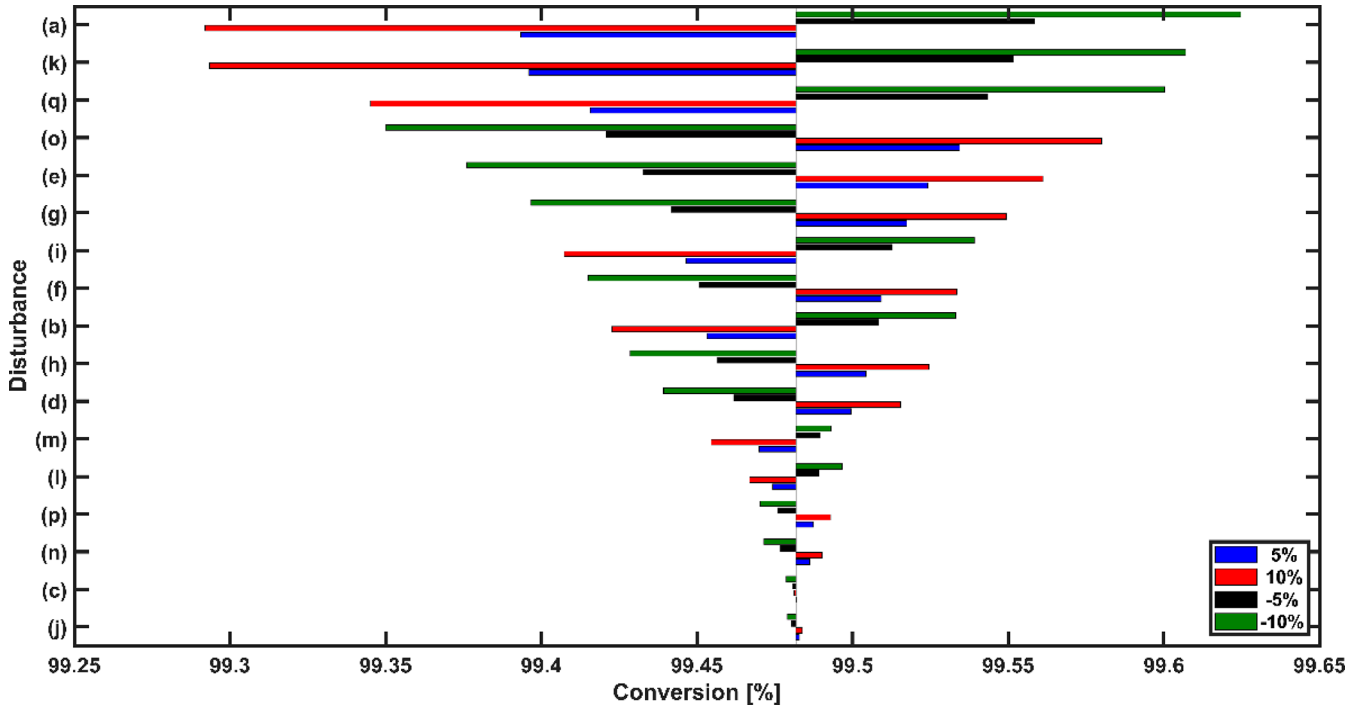

Figure 16. Tornado plot for conversion of the enone leaving CSTR3 as a function of the individual parameters: (a) enone flow rate, (b) enone concentration, (c) Mn catalyst flow rate, (d) Mn catalyst concentration, (e) flow rate of the hydrogen peroxide stream entering CSTR1, (f) concentration of the hydrogen peroxide stream entering CSTR2, (g) flow rate of the hydrogen peroxide stream entering CSTR2, (h) concentration of the hydrogen peroxide stream entering CSTR2, (i) CSTR1 temperature, (j) CSTR1 fill level, (k) CSTR2 temperature, (l) CSTR2 fill level, (m) CSTR3 temperature, (n) CSTR3 fill level, (o) pre-exponential factor for eq 1, (p) pre-exponential factor for eq 2, and (q) pre-exponential factor for eq 3.

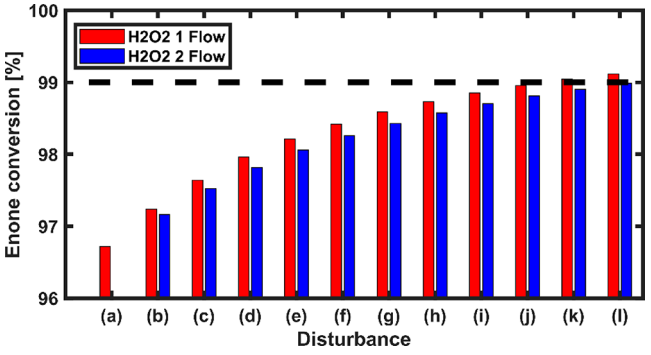

Figure 17. Recovery in conversion of the enone leaving CSTR3 starting with (a) the worst-case combination of disturbances followed by (b–l) increased hydrogen peroxide flow rate to CSTR1/CSTR2 at (b) nominal, (c) +10% of nominal, (d) +20% of nominal, (e) +30% of nominal, (f) +40% of nominal, (g) +50% of nominal, (h) +60% of nominal, (i) +70% of nominal, (j) +80% of nominal, (k) +90% of nominal, and (l) +100% of nominal.

series. A better strategy was determined to be the development of a feedback control strategy for online control of the conversion. Among the process variables with a strong impact on the conversion, the concentration and flow rate of the incoming enone could not be manipulated because this stream is produced upstream in the continuous manufacturing process. This left three options for manipulated variables: (1) the flow rate of the hydrogen peroxide stream entering CSTR1, (2) the flow rate of the hydrogen peroxide stream entering CSTR2, and (3) the temperature of CSTR2. As the epoxidation reaction is strongly exothermic, increasing the reaction temperature would not be desirable, as it would allow the opportunity for further degradation of hydrogen peroxide in the reactors and possibly a runaway reaction. As such, options (1) and (2) were investigated in Figure 17 by increasing the hydrogen peroxide flow rates incrementally by 10% at a time. In the unlikely scenario of the worst-case combination of all disturbances happening at the same time, an 80% increase in the hydrogen peroxide flow rate sent to CSTR1 and a 100% increase in the hydrogen peroxide flow rate sent to CSTR2 are required to maintain the target-level process specifications. The nominal hydrogen peroxide flow rate is ∼5% of the total flow rate entering CSTR1, so this increase will have minimal impacts on the residence time and downstream operation.

Chiral Purity of (*R*,*R*)-Epoxy Ketone Crystals Leaving MSMPR2. The step response matrices for the purity by weight of the (*R*,*R*)-epoxy ketone leaving MSMPR2 are shown in Figure 18. In general, this plot looks quite similar to Figure 15, which is to be expected. Specifically, the distribution coefficients in Figure 12 are quite large (∼0.6) for the enone and quite small (∼0.05) for the (*R*,*S*)-epoxy ketone. Thus, the greatest changes in purity should correlate to changes in the enone being fed to the MSMPR crystallizer, which explains the correlation. The other disturbances (changes in flows and concentrations after CSTR3) have a negligible impact on the purity, which shows that the process seems to be quite robust toward process disturbances. The relative ordering of the impacts of these disturbances and uncertainties on the product purity is shown in Figure 19.

In terms of developing a more robust process, the worst-case combination of all disturbances occurring at the same time is predicted to result in ∼96.7 wt % purity of the (*R*,*R*)-epoxy ketone prior to the wash protocol. This is quite close to the desired 97.5% purity, a value that was determined by correlation

https://dx.doi.org/10.1021/acs.oprd.0c00189
Org. Process Res. Dev. 2020, 24, 1891−1908

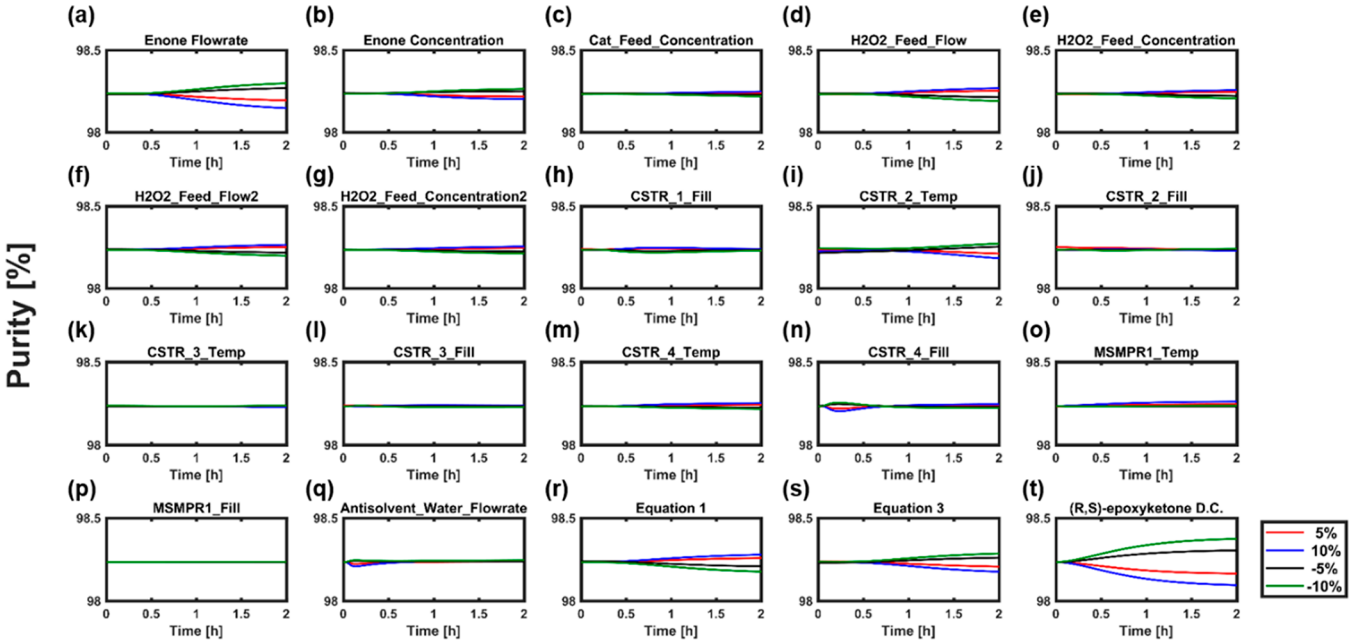

Figure 18. Purity of the (*R*,*R*)-epoxy ketone crystals leaving MSMPR2 as a function of changes in individual parameters: (a) enone flow rate, (b) enone concentration, (c) Mn catalyst concentration, (d) flow rate of the hydrogen peroxide stream entering CSTR1, (e) concentration of the hydrogen peroxide stream entering CSTR1, (f) flow rate of the hydrogen peroxide stream entering CSTR2, (g) concentration of the hydrogen peroxide stream entering CSTR2, (h) CSTR1 fill level, (i) CSTR2 temperature, (j) CSTR2 fill level, (k) CSTR3 temperature, (l) CSTR3 fill level, (m) CSTR4 temperature, (n) CSTR4 fill level, (o) MSMPR1 temperature, (p) MSMPR1 fill level, (q) antisolvent flow rate to MSMPR1, (r) eq 1 rate constant, (s) eq 3 rate constant, and (t) distribution coefficient for the (*R*,*S*)-epoxy ketone.

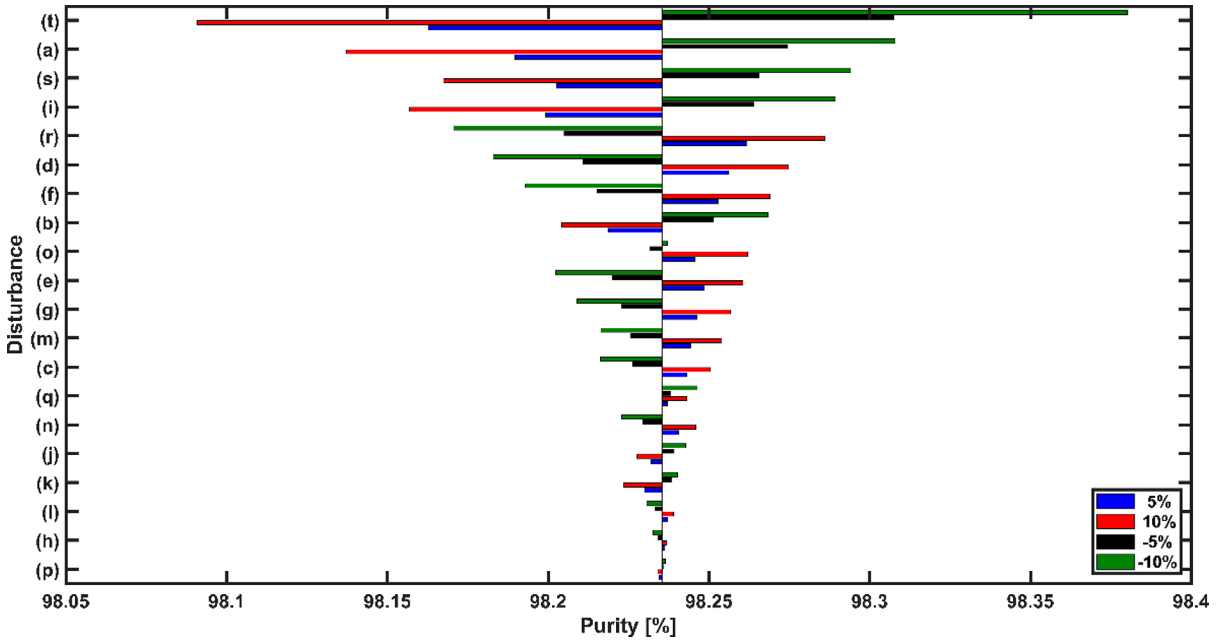

Figure 19. Tornado plot for the purity of the (*R*,*R*)-epoxy ketone crystals leaving MSMPR2 as a function of individual parameters ranked for their impact: (a) enone flow rate, (b) enone concentration, (c) Mn catalyst concentration, (d) flow rate of the hydrogen peroxide stream entering CSTR1, (e) concentration of the hydrogen peroxide stream entering CSTR1, (f) flow rate of the hydrogen peroxide stream entering CSTR2, (g) concentration of the hydrogen peroxide stream entering CSTR2, (h) CSTR1 fill level, (i) CSTR2 temperature, (j) CSTR2 fill level, (k) CSTR3 temperature, (l) CSTR3 fill level, (m) CSTR4 temperature, (n) CSTR4 fill level, (o) MSMPR1 temperature, (p) MSMPR1 fill level, (q) antisolvent flow rate to MSMPR1, (r) eq 1 rate constant, (s) eq 3 rate constant, and (t) distribution coefficient for the (*R*,*S*)-epoxy ketone.

to the desired chiral purity of 99.5% prior to dissolution in MTBE solution for final processing. This implies that minimal control strategy development may be needed. Because of the dependence on similar process disturbances observed in both Figures 18 and 15, the ability of the control strategy for enone conversion to suppress disturbances in purity was also investigated (Figure 20). As expected, this analysis revealed that the purity is more sensitive to these manipulated variables than the conversion (i.e., a smaller change in flow rate is required to reach the desired purity), so that one control strategy would

https://dx.doi.org/10.1021/acs.oprd.0c00189
Org. Process Res. Dev. 2020, 24, 1891−1908

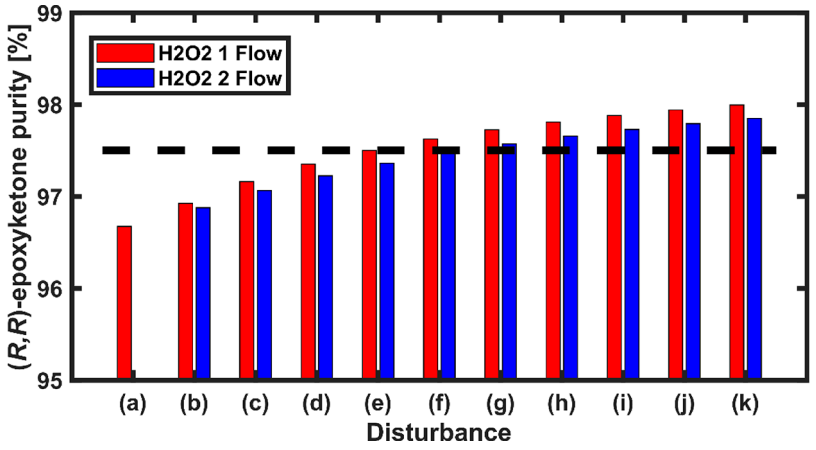

Figure 20. Recovery in the purity of the (*R*,*R*)-epoxy ketone leaving MSMPR2 for additive disturbances starting with (a) the worst-case combination of disturbances followed by (b–l) increased hydrogen peroxide flow rate to CSTR1/CSTR2 at (b) nominal, (c) +10% of nominal, (d) +20% of nominal, (e) +30% of nominal, (f) +40% of nominal, (g) +50% of nominal, (h) +60% of nominal, (i) +70% of nominal, (j) +80% of nominal, and (k) 90% of nominal.

be capable of satisfying both constraints. This exciting result implies that the crystallization CQA for purity is largely driven by removal of the primary reactant. Therefore, a well-designed and well-controlled upstream process is enough to guarantee satisfaction of the CQA for purity, which means that fewer higher-order control structures are required.

CONCLUSIONS

This article details the development of a virtual plant to characterize and develop process control strategies for the manufacture of (*R*,*R*)-epoxy ketone **2**, a carfilzomib drug substance intermediate, by an integrated continuous process involving eight unit operations. Individual unit operation models were built separately and then integrated into an end-to-end dynamic flowsheet model. This was subsequently used to determine the impact of process and model uncertainties on the process performance and product quality. The process was found to be sensitive to the expected disturbances and uncertainties, but the model was used to develop potential control strategies to mitigate the effects of these disturbances. This three-part series demonstrates the use of a virtual plant system to facilitate science- and risk-based implementation of continuous manufacturing practices that are in line with the ICH Q13 guidance goals.[36] This development process enabled the prediction of process performance and product quality in a real plant environment, which enables a truly agile process development paradigm. It is our hope that this work helps demonstrate both the technical feasibility and wide-reaching benefits of such a process development strategy and that it encourages others in the industry to consider similar approaches.

AUTHOR INFORMATION

Corresponding Author

Elçin Içten − *Process Development, Amgen, Inc., Cambridge, Massachusetts 02142, United States;* orcid.org/0000-0002-0962-7550; Email: eicten@amgen.com

Authors

Andrew J. Maloney − *Department of Chemical Engineering, Massachusetts Institute of Technology, Cambridge, Massachusetts 02139, United States;* orcid.org/0000-0002-9744-6433

Gerard Capellades − *Department of Chemical Engineering, Massachusetts Institute of Technology, Cambridge, Massachusetts 02139, United States;* orcid.org/0000-0002-4056-3823

Matthew G. Beaver − *Process Development, Amgen, Inc., Cambridge, Massachusetts 02142, United States;* orcid.org/0000-0003-3816-4601

Xiaoxiang Zhu − *Process Development, Amgen, Inc., Cambridge, Massachusetts 02142, United States*

Lauren R. Graham − *Process Development, Amgen, Inc., Cambridge, Massachusetts 02142, United States*

Derek B. Brown − *Process Development, Amgen, Inc., Thousand Oaks, California 91320, United States;* orcid.org/0000-0002-7909-0867

Daniel J. Griffin − *Process Development, Amgen, Inc., Cambridge, Massachusetts 02142, United States*

Rahul Sangodkar − *Process Development, Amgen, Inc., Cambridge, Massachusetts 02142, United States*

Ayman Allian − *Process Development, Amgen, Inc., Thousand Oaks, California 91320, United States*

Seth Huggins − *Process Development, Amgen, Inc., Thousand Oaks, California 91320, United States*

Roger Hart − *Process Development, Amgen, Inc., Cambridge, Massachusetts 02142, United States*

Pablo Rolandi − *Process Development, Amgen, Inc., Cambridge, Massachusetts 02142, United States*

Shawn D. Walker − *Process Development, Amgen, Inc., Cambridge, Massachusetts 02142, United States;* orcid.org/0000-0001-8827-4679

Richard D. Braatz − *Department of Chemical Engineering, Massachusetts Institute of Technology, Cambridge, Massachusetts 02139, United States;* orcid.org/0000-0003-4304-3484

Complete contact information is available at: https://pubs.acs.org/10.1021/acs.oprd.0c00189

Notes

The authors declare no competing financial interest.

ACKNOWLEDGMENTS

Authors acknowledge Meera Mahadevan, Ananya Chowdhury, and Kevin Healy from Process Systems Enterprise Ltd. for their support on gPROMS models. The contribution of A.J.M. was partially supported by the National Science Foundation

Graduate Research Fellowship under Grant 1122374. Any opinion, findings, and conclusions or recommendations expressed in this material are those of the authors(s) and do not necessarily reflect the views of the National Science Foundation.

■ ABBREVIATIONS

ACN, acetonitrile; AcOH, acetic acid; CM, continuous manufacturing; PP, process parameter; CQA, critical quality attribute; CSTR, continuously stirred tank reactor; DEC, decanter; FBRM, focused beam reflectance measurement; GC, gas chromatography; H_2O_2, hydrogen peroxide; HPLC, high-performance liquid chromatography; IR, infrared spectroscopy; KF, Karl Fischer; LLE, liquid−liquid extraction; MSMPR, mixed-suspension mixed-product-removal; MTBE, methyl *tert*-butyl ether; $NaHSO_3$, sodium bisulfite; UPLC, ultraperformance liquid chromatography; XRPD, X-ray powder diffraction

■ REFERENCES

(1) Schaber, S. D.; Gerogiorgis, D. I.; Ramachandran, R.; Evans, J. M. B.; Barton, P. I.; Trout, B. L. Economic Analysis of Integrated Continuous and Batch Pharmaceutical Manufacturing: A Case Study. *Ind. Eng. Chem. Res.* **2011**, *50* (17), 10083−10092.

(2) Srai, J. S.; Badman, C.; Krumme, M.; Futran, M.; Johnston, C. Future Supply Chains Enabled by Continuous Processing-Opportunities and Challenges May 20−21, 2014 Continuous Manufacturing Symposium. *J. Pharm. Sci.* **2015**, *104* (3), 840−849.

(3) Lee, S. L.; O'Connor, T. F.; Yang, X.; Cruz, C. N.; Chatterjee, S.; Madurawe, R. D.; Moore, C. M. V.; Yu, L. X.; Woodcock, J. Modernizing Pharmaceutical Manufacturing: From Batch to Continuous Production. *J. Pharm. Innovation* **2015**, *10*, 191−199.

(4) Içten, E.; Nagy, Z. K.; Reklaitis, G. V. Process Control of a Dropwise Additive Manufacturing System for Pharmaceuticals Using Polynomial Chaos Expansion Based Surrogate Model. *Comput. Chem. Eng.* **2015**, *83*, 221−231.

(5) Rakita, P. E. Safe Handling Practices of Industrial Scale Grignard Reagents. In *Handbook of Grignard Reagents*; Silverman, G. S., Rakita, P. E., Eds.; CRC Press, 1996; Chapter 5, pp 79−88.

(6) He, W.; Fang, Z.; Ji, D.; Chen, K.; Wan, Z.; Li, X.; Gan, H.; Tang, S.; Zhang, K.; Guo, K. Epoxidation of Soybean Oil by Continuous Micro-Flow System with Continuous Separation. *Org. Process Res. Dev.* **2013**, *17* (9), 1137−1141.

(7) Lakerveld, R.; Benyahia, B.; Braatz, R. D.; Barton, P. I. Model-Based Design of a Plant-Wide Control Strategy for a Continuous Pharmaceutical Plant. *AIChE J.* **2013**, *59* (10), 3671−3685.

(8) Içten, E.; Giridhar, A.; Taylor, L. S.; Nagy, Z. K.; Reklaitis, G. V. Dropwise Additive Manufacturing of Pharmaceutical Products for Melt-Based Dosage Forms. *J. Pharm. Sci.* **2015**, *104* (5), 1641−1649.

(9) Ramachandran, R.; Arjunan, J.; Chaudhury, A.; Ierapetritou, M. G. Model-Based Control-Loop Performance of a Continuous Direct Compaction Process. *J. Pharm. Innovation* **2011**, *6* (4), 249−263.

(10) Myerson, A. S.; Krumme, M.; Nasr, M.; Thomas, H.; Braatz, R. D. Control Systems Engineering in Continuous Pharmaceutical Manufacturing May 20−21, 2014 Continuous Manufacturing Symposium. *J. Pharm. Sci.* **2015**, *104* (3), 832−839.

(11) Içten, E.; Reklaitis, G. V.; Nagy, Z. K. Advanced Control for the Continuous Dropwise Additive Manufacturing of Pharmaceutical Products. *Comput.-Aided Chem. Eng.* **2018**, *41*, 379−401.

(12) Icten, E.; Maloney, A. J.; Beaver, M. G.; Shen, D. E.; Zhu, X.; Graham, L. R.; Robinson, J. A.; Huggins, S.; Allian, A. D.; Hart, R.; et al. A Virtual Plant for Integrated Continuous Manufacturing of a Carfilzomib Drug Substance Intermediate, Part 1: CDI-Promoted Amide Bond Formation. *Org. Process Res. Dev.* **2020**, DOI: 10.1021/acs.oprd.0c00187.

(13) Icten, E.; Maloney, A. J.; Beaver, M. G.; Zhu, X.; Shen, D. E.; Robinson, J. A.; Parsons, A. T.; Allian, A. D.; Huggins, S.; Hart, R.; et al. A Virtual Plant for Integrated Continuous Manufacturing of a Carfilzomib Drug Substance Intermediate, Part 2: Enone Synthesis via a Barbier-Type Grignard Process. *Org. Process Res. Dev.* **2020**, DOI: 10.1021/acs.oprd.0c00188.

(14) Lane, B. S.; Burgess, K. Metal-Catalyzed Epoxidations of Alkenes with Hydrogen Peroxide. *Chem. Rev.* **2003**, *103* (7), 2457−2473.

(15) Grigoropoulou, G.; Clark, J. H.; Elings, J. A. Recent Developments on the Epoxidation of Alkenes Using Hydrogen Peroxide as an Oxidant. *Green Chem.* **2003**, *5* (1), 1−7.

(16) Rangarajan, B.; Havey, A.; Grulke, E. A.; Culnan, P. D. Kinetic Parameters of a Two-Phase Model for in Situ Epoxidation of Soybean Oil. *J. Am. Oil Chem. Soc.* **1995**, *72* (10), 1161−1169.

(17) Hage, R.; Iburg, J. E.; Kerschner, J.; Koek, J. H.; Lempers, E. L. M.; Martens, R. J.; Racherla, U. S.; Russell, S. W.; Swarthoff, T.; Van Vliet, M. R. P.; et al. Efficient Manganese Catalysts for Low-Temperature Bleaching. *Nature* **1994**, *369* (6482), 637−639.

(18) Alvarez, A. J.; Singh, A.; Myerson, A. S. Crystallization of Cyclosporine in a Multistage Continuous MSMPR Crystallizer. *Cryst. Growth Des.* **2011**, *11* (10), 4392−4400.

(19) Li, J.; Trout, B. L.; Myerson, A. S. Multistage Continuous Mixed-Suspension, Mixed-Product Removal (MSMPR) Crystallization with Solids Recycle. *Org. Process Res. Dev.* **2016**, *20* (2), 510−516.

(20) Mascia, S.; Heider, P. L.; Zhang, H.; Lakerveld, R.; Benyahia, B.; Barton, P. I.; Braatz, R. D.; Cooney, C. L.; Evans, J. M. B.; Jamison, T. F.; et al. End-to-End Continuous Manufacturing of Pharmaceuticals: Integrated Synthesis, Purification, and Final Dosage Formation. *Angew. Chem., Int. Ed.* **2013**, *52* (47), 12359−12363.

(21) Cole, K. P.; Groh, J. M. C.; Johnson, M. D.; Burcham, C. L.; Campbell, B. M.; Diseroad, W. D.; Heller, M. R.; Howell, J. R.; Kallman, N. J.; Koenig, T. M.; et al. Kilogram-Scale Prexasertib Monolactate Monohydrate Synthesis under Continuous-Flow CGMP Conditions: Supplement. *Science* **2017**, *356* (6343), 1144−1151.

(22) Acevedo, D.; Jarmer, D. J.; Burcham, C. L.; Polster, C. S.; Nagy, Z. K. A Continuous Multi-Stage Mixed-Suspension Mixed-Product-Removal Crystallization System with Fines Dissolution. *Chem. Eng. Res. Des.* **2018**, *135*, 112−120.

(23) Liu, Y. C.; Domokos, A.; Coleman, S.; Firth, P.; Nagy, Z. K. Development of Continuous Filtration in a Novel Continuous Filtration Carousel Integrated with Continuous Crystallization. *Org. Process Res. Dev.* **2019**, *23*, 2655.

(24) Beaver, M.; Shi, X.; Riedel, J.; Patel, P.; Zeng, A.; Corbett, M.; Robinson, J. A.; Parsons, A.; Cui, S.; Baucom, K.; et al. Continuous Process Improvement in the Manufacture of Carfilzomib, Part 2: An Improved Process for Synthesis of the Epoxyketone Warhead. *Org. Process Res. Dev.* **2020**, *24* (4), 490−499.

(25) Hu, W. F.; Zhao, J. Q.; Chen, Y. Z.; Zhang, X. M.; Xu, X. Y.; Yuan, W. C. Organocatalyzed Enantioselective Conjugated Addition of Sodium Bisulfite to β-Trifluoromethyl-α,β-Unsaturated Ketones. *J. Org. Chem.* **2018**, *83* (10), 5771−5777.

(26) Hou, G.; Power, G.; Barrett, M.; Glennon, B.; Morris, G.; Zhao, Y. Development and Characterization of a Single Stage Mixed-Suspension, Mixed-Product-Removal Crystallization Process with a Novel Transfer Unit. *Cryst. Growth Des.* **2014**, *14* (4), 1782−1793.

(27) Randolph, A. D.; Larson, M. A. *Theory of Particulate Processes: Analysis and Techniques of Continuous Crystallization*; Academic Press, 1971.

(28) Capellades, G.; Wiemeyer, H.; Myerson, A. S. Mixed-Suspension, Mixed-Product Removal Studies of Ciprofloxacin from Pure and Crude Active Pharmaceutical Ingredients: The Role of Impurities on Solubility and Kinetics. *Cryst. Growth Des.* **2019**, *19* (7), 4008−4018.

(29) Lai, T. T. C.; Cornevin, J.; Ferguson, S.; Li, N.; Trout, B. L.; Myerson, A. S. Control of Polymorphism in Continuous Crystallization via Mixed Suspension Mixed Product Removal Systems Cascade Design. *Cryst. Growth Des.* **2015**, *15* (7), 3374−3382.

(30) Li, J.; Lai, T. T. C.; Trout, B. L.; Myerson, A. S. Continuous Crystallization of Cyclosporine: Effect of Operating Conditions on Yield and Purity. *Cryst. Growth Des.* **2017**, *17* (3), 1000−1007.

(31) Murugesan, S.; Hallow, D. M.; Vernille, J. P.; Tom, J. W.; Tabora, J. E. Lean Filtration: Approaches for the Estimation of Cake Properties. *Org. Process Res. Dev.* **2012**, *16* (1), 42−48.

(32) Huggins, S.; Cosbie, A.; Gaertner, J. Filtration Case Studies. *Chem. Eng. Pharm. Ind.* **2019**, 833−845.
(33) Process Systems Enterprise. *gPROMS FormulatedProducts*. https://www.psenterprise.com/products/gproms/formulatedproducts (accessed 2020-04-15).
(34) *MATLAB and Simulink*; The Mathworks: Natick, MA, 2016.
(35) *DynoChem Resources*. https://dcresources.scale-up.com (accessed 2020-04-15).
(36) *Final Concept Paper for ICH Q13: Continuous Manufacturing of Drug Substances and Drug Products*. International Council for Harmonisation, November 14, 2018. https://database.ich.org/sites/default/files/Q13_EWG_Concept_Paper.pdf (accessed 2020-04-15).

https://dx.doi.org/10.1021/acs.oprd.0c00189
Org. Process Res. Dev. 2020, 24, 1891−1908